# LATTICE DISTORTIONS OF $V_2O_3$ THIN FILMS DURING METAL-TO-INSULATOR TRANSITION

A Thesis

Presented to the Faculty of the Graduate School

of Cornell University

In Partial Fulfillment of the Requirements for the Degree of

Master of Science

by

Ziming Shao

August 2019

© 2019 Ziming Shao

# ABSTRACT

As a prototypical Mott-Hubbard system, bulk vanadium sesquioxide ($V_2O_3$), undergoes a first-order Metal-to-Insulator Transition (MIT) from the paramagnetic metallic phase to an antiferromagnetic insulator phase upon cooling to ~160K. Along with MIT, a structural phase transition from rhombohedral to monoclinic structure happens around the same temperature. In the past few decades, the transition temperature of $V_2O_3$ has been successfully modified by tens of degrees by introducing lattice strain (through doping, heteroepitaxial growth, etc.). However, how the lattice strain affects the structural distortion and MIT remains elusive to this day. In this work, we studied the lattice distortion of $V_2O_3$ thin films heteroepitaxially grown on variously oriented sapphire substrates through X-ray diffraction at Cornell High Energy Synchrotron Source (CHESS). We show that the in-plane biaxial strain drastically affects the intrinsic lattice distortions and the microstrain states in films. Besides, an intermediate interfacial structure was observed in the film grown on (100)-oriented substrate, which is a plausible model for explaining the recent discovery of a memory effect in electrical transport properties of $V_2O_3$.

# TABLE OF CONTENTS

# INTRODUCTION

## *Vanadium Sesquioxide*

Bulk $V_2O_3$ has a rhombohedral structure with symmetry of $R\bar{3}c$ at room temperature and distorts to a less symmetrical monoclinic structure with symmetry of I2/a at ~160K. The corresponding lattice parameters[1] are shown in Table 1.1.

| | a/Å | b/Å | c/Å | γ, β /degree |
|---|---|---|---|---|
| Rhombohedral | 4.9537(2) | | 14.0111(6) | 120 |
| Monoclinic | 7.2727(4) | 5.0027(3) | 5.5432(3) | 96.762(2) |

Table 1.1

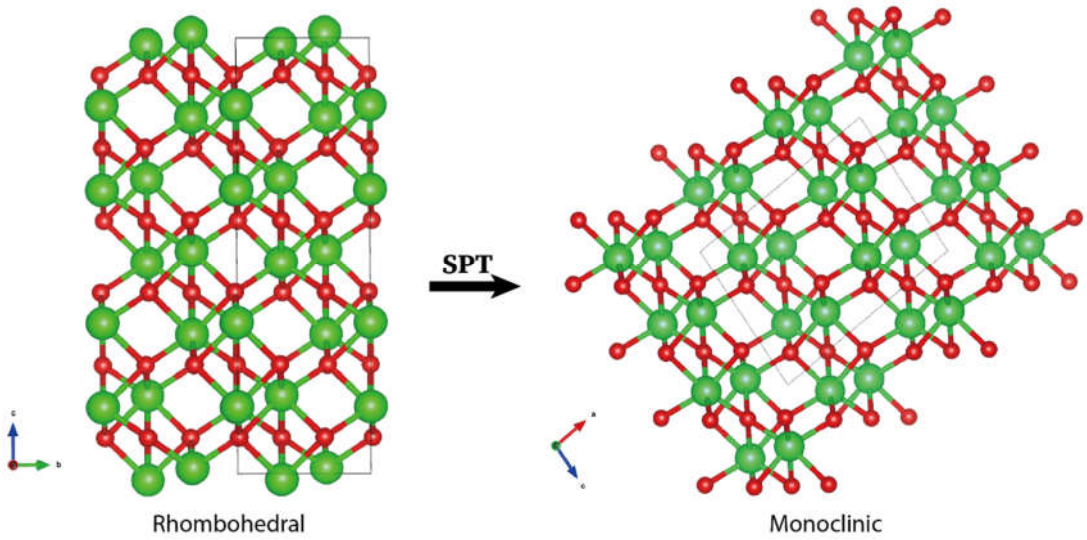


Figure 1.1
The structures of rhombohedral metallic and monoclinic insulating Vanadium Sesquioxide. The green atoms represent for vanadium and red for oxygen. The rhombohedral and monoclinic lattices are aligned according to Dernier[2].

During the structural phase transition (SPT), the c-axis in the hexagonal cell tilts ~1.8 degrees towards the hexagonal basal plane along the direction of three equivalent

rhombohedral-cell directions[2], such as ($\bar{1}$10), (010) and ($\bar{1}$00). Moreover, the probability of the three tilts in an ideal crystal should be the same to each other; in other words, the lattice distortion exhibits a triple twinning. After the distortion, the (110) axes in rhombohedral indexed cell transform into the unique (010) axes in the monoclinic cell. And for any other given hexagonal axis, the corresponding appropriate monoclinic indexes could be derived using the following three matrixes[2].

$$\begin{bmatrix} \frac{2}{3} & \frac{4}{3} & \frac{1}{3} \\ 1 & 0 & 0 \\ \frac{1}{3} & \frac{2}{3} & \frac{-1}{3} \end{bmatrix} \begin{bmatrix} \frac{-4}{3} & \frac{-2}{3} & \frac{1}{3} \\ 0 & 1 & 0 \\ \frac{-2}{3} & \frac{-1}{3} & \frac{-1}{3} \end{bmatrix} \begin{bmatrix} \frac{2}{3} & \frac{-2}{3} & \frac{1}{3} \\ -1 & -1 & 0 \\ \frac{1}{3} & \frac{-1}{3} & \frac{-1}{3} \end{bmatrix}$$

In addition to the structural phase transition, there is also a Metal-to-Insulator Transition (MIT) happens at a similar temperature range, which is widely regarded as a prototypical realization of a genuine Mott-Hubbard transition[3] (as shown in Fig. 1.2). During the MIT, the vanadium sesquioxide undergoes a transition from a paramagnetic metallic state to an antiferromagnetic insulator state[4].

The MIT occurs with varying temperature and pressure, and in the past few decades, researchers successfully modified the transition temperature by introducing lattice strain through applying hydrostatic pressure, doping[1,4,5], or heteroepitaxial growth[6–9]. Especially when doped with transition metals such as Cr or Ti, the MIT of vanadium sesquioxide could even be suppressed where the metallic phase can be stabilized with Ti doping and the insulating phase with Cr doping[1]. However, despite the enormous

amount of research, the mechanism behind the MIT of $V_2O_3$ and the correlation between the MIT and SPT remain elusive to this day.

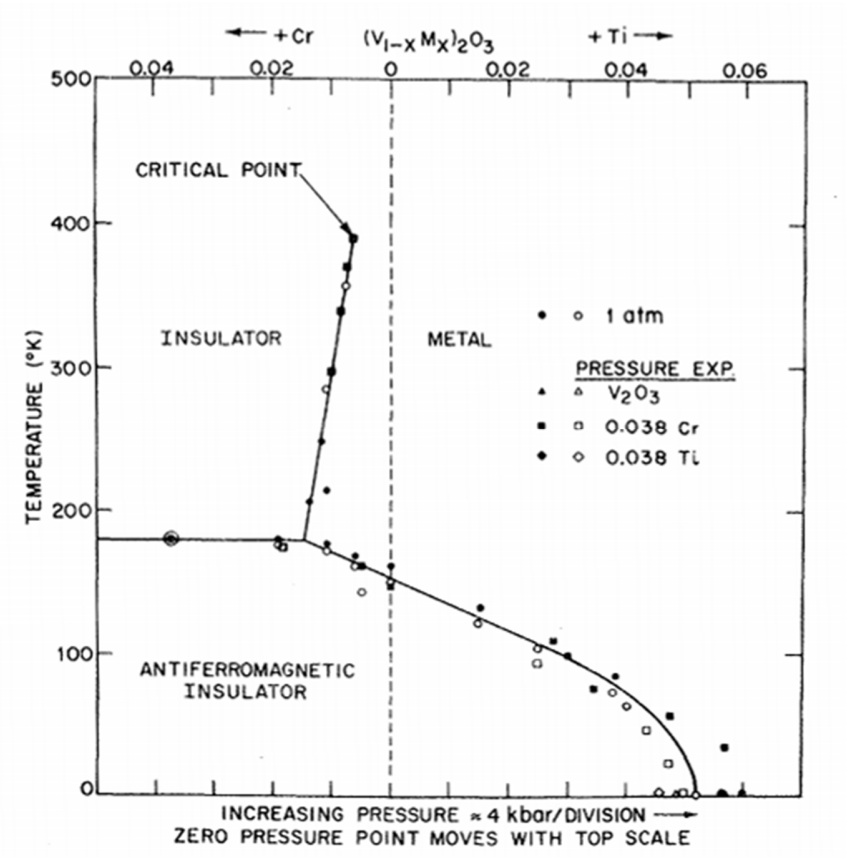


Figure 1.2
The phase diagram for bulk $V_2O_3$

Promisingly, with the development of characterization techniques, more perspectives are provided to the researchers to pursue the essence of this problem. Recently, the real space nanotextured phase coexistence of vanadium sesquioxide thin film during MIT is studied with the cryogenic nearfield infrared microscopy[10]. In the study, the authors observed the coexistence of metallic and correlated insulator phase with percolation and inferred the decoupling of the MIT and SPT, which challenged the conventional picture of this strongly correlated electron system. However, due to the films' depth-dependent

domain evolution and the limited penetration depth of IR, their findings are under strong contradiction[11], which requires further examination.

In addition to the correlation of the SPT and MIT, another recent enlightening progress about vanadium sesquioxide is its ramp-reversal memory. The ramp-reversal memory was first discovered by Naor Vardi in $VO_2$ and revealed by an increase of resistance at a specific temperature, which is set by reversing the temperature ramp from heating to cooling during the MIT[12]. As a closely related compound of $VO_2$, the ramp-reversal memory was also exanimated and discovered in $V_2O_3$ thin films. The ramp-reversal memory indicates the existence of a structural phase-boundary scar, which provides a new route to control the electrical transport properties of $V_2O_3$. Further investigations are in urgent need to experimentally observe the structural scars.

Moreover, the dynamics and the mesoscale heterogeneity of $V_2O_3$ during the MIT were studied with ultrafast X-ray scattering and X-ray nano-diffraction recently[13]. The phase coexistence of structural domains was revealed by the nano-diffraction studies. Furthermore, they found also the low temperature phase consists of nanotwins about 8 nm in size. Only two out of three possible twins were observed on the R-$(012)_R$ oriented samples.

## *X-Ray Diffraction*

X-ray diffraction is one of the most widely used materials structural characterization method. Since the discovery of X-ray radiation by Röntgen in 1895, the brilliance of X-ray sources has been enhanced dramatically[14] (as shown in Figure 1.3), which allows the sufficient data to be collected in an extremely short time and greatly improve the competence of X-ray diffraction.

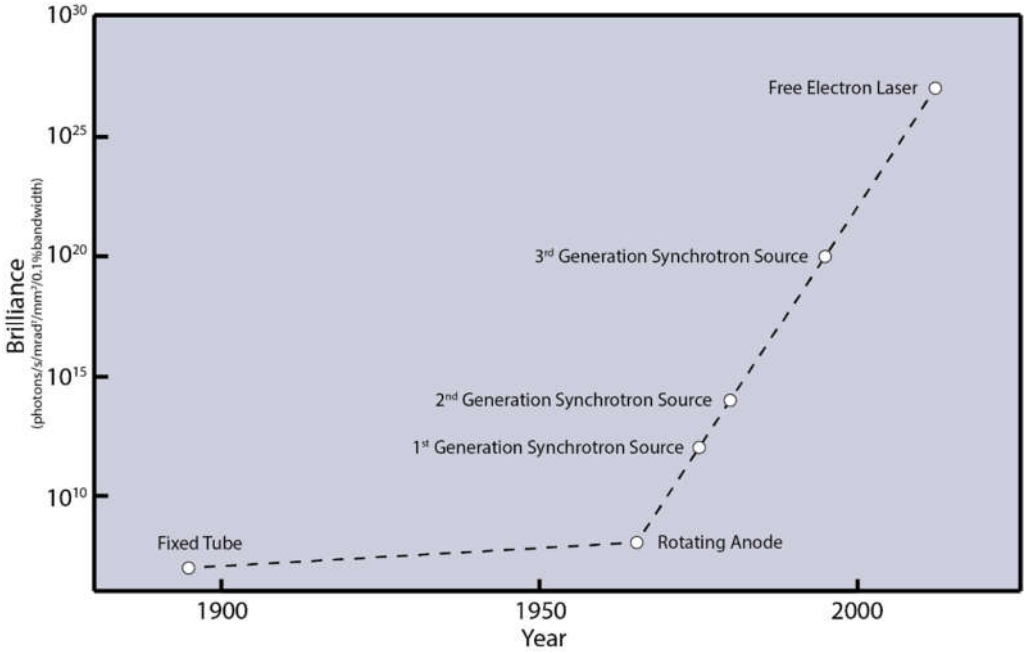


Figure 1.3
Evolution of X-ray source brilliance

The essential of X-ray diffraction is based on the scattering of photons by electrons. For a periodic structure in crystalline materials, the scattering factor is defined as

$$F_{crystal}(Q) = \sum_{j} \mathrm{f_j(Q)}\, \mathrm{e}^{\mathrm{i}\boldsymbol{Qr_j}} \sum_{\mathrm{n}} \mathrm{e}^{\mathrm{i}\boldsymbol{QR_n}}$$

The first term is known as the unit cell structure factor, where $f_j$ is the atomic form factor of the $j^{th}$ atom in the unit cell, $\mathbf{r_j}$ is the atom vector. And the second term is lattice sum, where $\mathbf{R_n}$ is the lattice vector and **Q** is the scattering vector. The scattering factor **Q** is defined as $\boldsymbol{Q} = \boldsymbol{K_{out}} - \boldsymbol{K_{in}}$, where $\boldsymbol{K_{in}}$ and $\boldsymbol{K_{out}}$ have a direction of the incident and scattered beam respectively, and $|\boldsymbol{K_{in}}|=|\boldsymbol{K_{out}}|=2\pi/\lambda$. It is worth noticing, all the terms in the lattice sum are phase factors located on the unit circle in the complex plane. Therefore, the lattice sum will be order of unity unless it happens to fulfill

$$\boldsymbol{Q} = \mathrm{h}\boldsymbol{a}^* + \mathrm{k}\boldsymbol{b}^* + \mathrm{l}\boldsymbol{c}^*$$

where $\boldsymbol{a}^*$, $\boldsymbol{b}^*$, $\boldsymbol{c}^*$ are reciprocal lattice basis vectors, which could be defined by the basis vectors of the lattice $\boldsymbol{a}$, $\boldsymbol{b}$, $\boldsymbol{c}$. For example, $\boldsymbol{a}^* = 2\pi\frac{\boldsymbol{b}\times\boldsymbol{c}}{\boldsymbol{a}\cdot(\boldsymbol{b}\times\boldsymbol{c})}$. Then, $\boldsymbol{Q}\cdot\boldsymbol{R_n} = 2\pi\cdot\text{integer}$ and the lattice sum becomes order of N (the number of unit cells). This is called the Laue condition, which is identical to the Bragg's law, $n\lambda=2d\cdot\sin(\theta)$.

Another important concept we use in this thesis is the Ewald sphere, as introduced above, $\boldsymbol{Q} = \boldsymbol{K_{out}} - \boldsymbol{K_{in}}$. For a monochromatic beam, the length of $\boldsymbol{K_{in}}$ and $\boldsymbol{K_{out}}$ are constant $2\pi/\lambda$. If the direction of the incident beam is fixed, the possible $\boldsymbol{Q}$ vectors are shown in Fig. 1.4, which all falls on a sphere, namely, the Ewald sphere. In other words, without changing the incident beam and the sample's position, the Ewald sphere is all the section we can use X-ray diffraction to analyze in the reciprocal space.

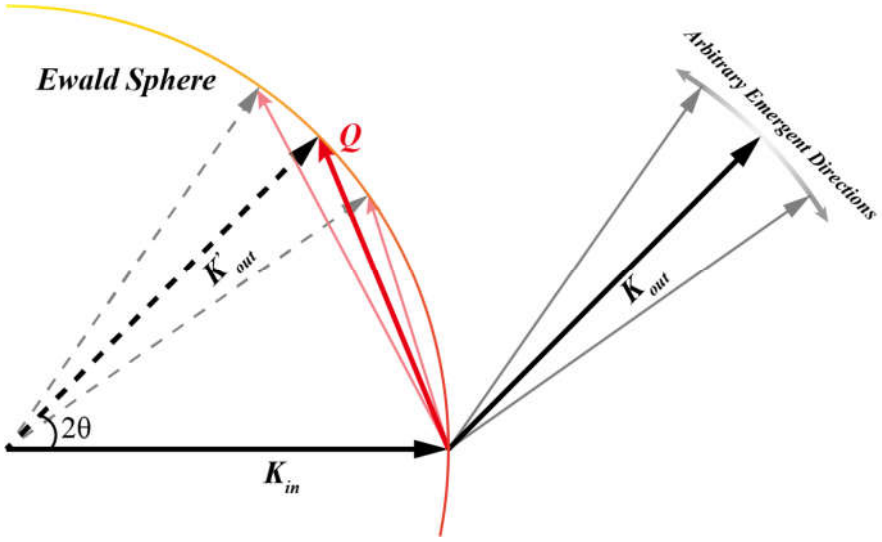


Figure 1.4
Illustration of the Ewald sphere

However, in practice, the diffraction pattern is seldom a very sharp peak. Instead, the peaks are usually broadened in reciprocal space by many reasons, such as finite instrumental resolution, microstructural defects, sample deformation, lattice misorientation, limited coherently scattering domain size and microstrain, etc[15]. Neglecting the instrumental limitation, which is much improved at synchrotron sources, the broadening of the Bragg peak along $\boldsymbol{Q}$ is mainly caused by the microstrain and the limited coherently scattering domain size, mosaicity, in the $\boldsymbol{Q}$ direction. And the broadening normal to $\boldsymbol{Q}$ is mainly caused by crystal misalignment and limited coherently scattering domain size.

The atomic form factor is calculated by

$$f(\boldsymbol{Q}) = \int \rho(\boldsymbol{r}) e^{i\boldsymbol{Q}\boldsymbol{r}} d\boldsymbol{r}$$

which is recognized as a Fourier transformation. In other words, the diffraction pattern in reciprocal space is related to the real structure electron density distribution by Fourier transformation. Therefore, reciprocal diffraction pattern for a perfect enormous crystal is a sharp spot, and for a 2D film is a rod perpendicular to it. In other words, the diffraction pattern broadens in the direction of the limited coherently scattering domain size. Scherrer equation relates the peak broadening and limited coherently scattering domain size and widely used to calculate the average crystal size in powder diffraction.

$$\mathrm{L} = \frac{K\lambda}{\beta cos\theta}$$

where $K$ is the shape factor, $\lambda$ is the beam wavelength, $\beta$ is the integral peak width (broadening), and $\theta$ is the Bragg angle. The shape factor is usually around 1 and changes with the shape of the small crystals.

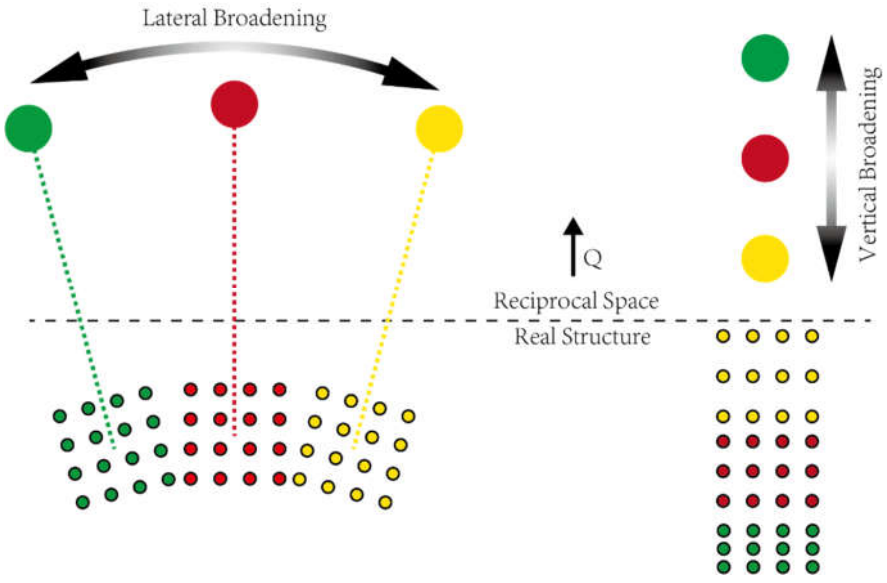


Figure 1.5
Illustration of the peak broadenings caused by misalignment and microstrain.
The misalignment and microstrain can cause the lateral and vertical peak broadening respectively.

As the rotation of the real structure will also result in the rotation of the reciprocal space, the broadening caused by misalignment is straightforward, as shown in Fig. 1.5. However, the concept of microstrain is more complex and should be carefully distinguished from strain. The microstrain describes the variance of strain states in a structure, which is not related to the absolute strain value. In other words, for a structure heavily strained, its microstrain could still be negligible, as long as the strain is uniform everywhere. The microstrain is correlated to the variance of lattice distance, which could be directly reflected in the peak broadening in reciprocal space.

In practice, all the broadening factors are convoluted together into a single measured peak width, and the separation of the broadening due to each factor is difficult. Without knowing the crystallize size and misorientation, the deconvolution is impossible from a single peak; deconvolution is possible with measuring multiple peaks as proposed by Warren[16] and Williamson-Hall[17]. In the Williamson-Hall method, the most common assumption is that the peak shape is either Gaussian or Lorentzian, and the broadening factors are convoluted together in the following ways respectively[15].

$$\beta_{Lorentzian} = \beta_{Microstrain} + \beta_{Size}$$

$$\beta^2_{Gaussian} = \beta^2_{Microstrain} + \beta^2_{Size}$$

where $\beta$ is the integral breadths of the broadening. Furthermore, the broadening due to limited coherently scattering domain is not sensitive to the peak's distance from the reciprocal origin (length of $\boldsymbol{Q}$). However, the microstrain exhibits linear relation with the length of $\boldsymbol{Q}$. Therefore, if we plot the integral breadth as a function of the length of $\boldsymbol{Q}$, we can use a linear fit to separate the broadening factors, as illustrated in Fig 1.6.

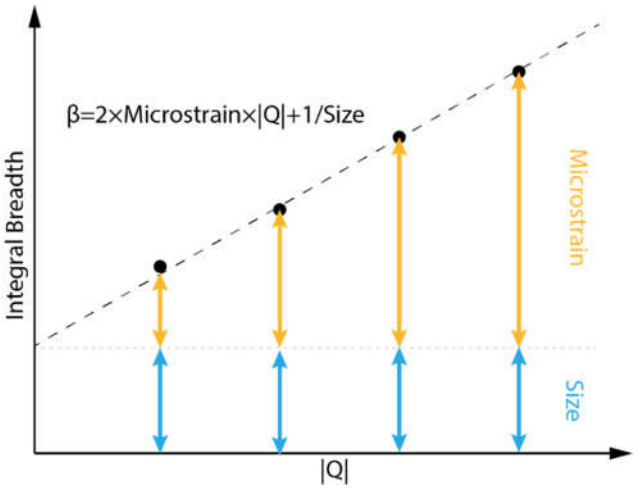


Figure 1.6
Illustration of the Williamson-Hall plot

# EXPERIMENTAL

3D-reciprocal space of selected Bragg peaks was measured in in-situ X-ray diffraction experiments at CHESS to perform further Williamson-Hall analysis.

## *Sample Preparation*

The $V_2O_3$ thin films are grown on sapphire substrates with the orientations of (012) R-plane, (100) M-plane or (110) A-plane (as shown in Fig. 2.1) in high-vacuum sputter deposition system with a base pressure of $1 \times 10^{-7}$ Torr by our colleagues in Ivan Schuller's group at UC San Diego[11]. The thickness of the films is approximately 300nm.

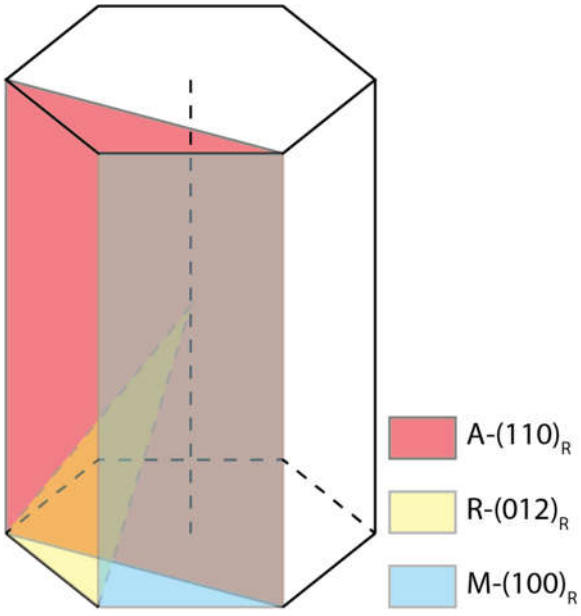


Figure 2.1
Illustration of the crystallographic planes for different oriented substrates

To realize accurate temperature measurement and control, we maximized the thermal conductivity between the thermometer and films by mounting samples with copper sample holders and copper tape. Meanwhile, to perform in-situ four-probe resistivity

measurement, we attached four wires with low temperature resistant insulating coatings to the surfaces of films through welding with silver-indium solder. The sample was mounted on the cryostat under vacuum.

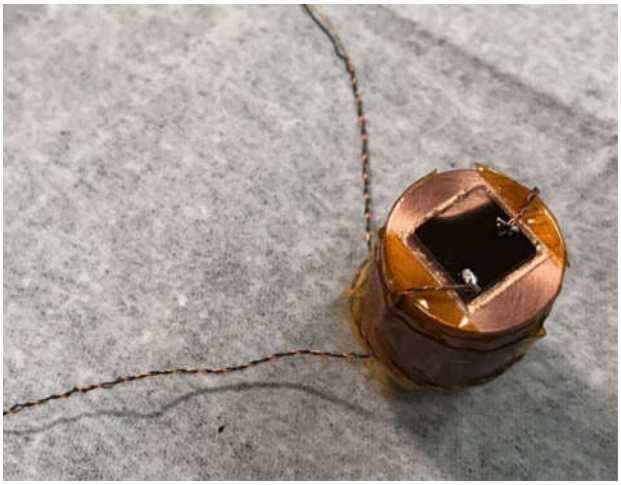

Figure 2.2
Sample ready to mount.
Kapton tape is used to fix wires under the low-temperature vacuum condition.

## *In-situ X-Ray Diffraction*

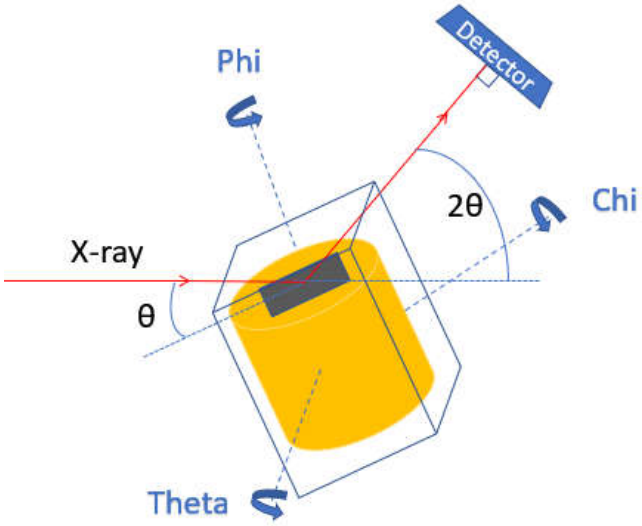


Figure 2.3
Illustration of experiment setup
The distance from sample to the center of 2-D detector is about 0.559m. The span of 2θ is about 0-75 degree.

The X-ray diffraction was performed at Cornell High Energy Synchrotron Source (CHESS) A2 station with the beam energy tuned to 14.488keV. During theta-scan we fixed the position of detector and the direction of the incoming beam (Fig. 2.3). We collected 3D reciprocal space maps by rocking the crystal and collecting 2D diffraction patterns using the Pilatus detector (Fig. 2.4). We performed the X-ray diffraction and resistivity measurement with the four-probe method using Keithley 2400 while continuously changing the temperature in 2.5K steps through the transition.

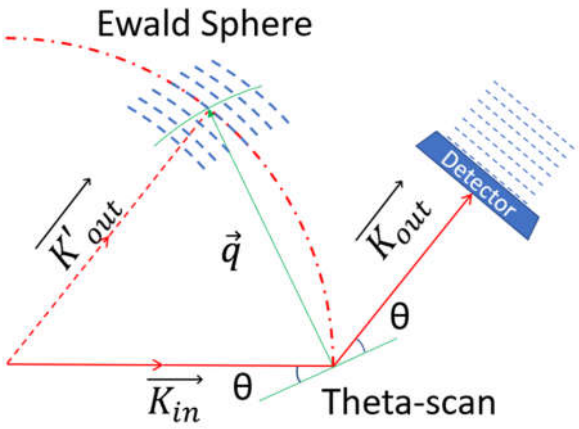


Figure 2.4
Collecting 3D reciprocal space information by theta-scan

For films with different orientations, various in-plane and out-of-plane peaks were measured. The measured theta range, steps and exposure time of each peak are listed as the following table.

| Substrate Orientation | Diffraction Planes | Chi (degree) | Theta Range (degree) | Step (degree) | Exposure Time (s) |
|---|---|---|---|---|---|
| A-300nm | (110) | 0 | 8 | 0.16 | 0.4 |
| | (220) | | 6 | 0.12 | 0.4 |
| | (330) | | 4 | 0.08 | 0.4 |
| | (012) | 42.4 | 8 | 0.16 | 0.4 |
| | (024) | | 6 | 0.12 | 0.4 |
| | (036) | | 4 | 0.08 | 0.4 |
| | (048) | | 3 | 0.06 | 0.4 |
| R-300nm | (012) | 0 | 5 | 0.05 | 0.2 |
| | (024) | | 5 | 0.05 | 0.2 |
| | (036) | | 4.2 | 0.042 | 0.4 |
| | (048) | | 4.4 | 0.044 | 0.6 |
| M-300nm | (300) | 0 | 4 | 0.08 | 0.4 |
| | (600) | | 5 | 0.1 | 0.4 |
| | (012) | 33 | 4 | 0.8 | 0.4 |
| | (024) | | 4 | 0.8 | 0.4 |
| | (036) | | 4 | 0.8 | 0.4 |
| | (048) | | 4 | 0.8 | 0.4 |

Table 2.1
Summary of experiment parameters

## *3D Reciprocal Space Reconstruction*

As introduced in chapter one, by transforming each image captured by a 2D detector, we could get a section of the Ewald sphere in reciprocal space. Based on a method used in ref [18], we developed a program to interpolate the diffraction intensities measured by a 2theta tilted 2D detector onto a regular 3D cartesian grid in the reciprocal space. For each pixel placed at vector $\vec{p}$ (referenced to the center of the detector), it could be indexed as (I, J) according to the relationship $\vec{p} = s(I\vec{\imath}, J\vec{\jmath})$ , in which s is the square pixel size and *i j* are the unit vectors. (as shown in Fig. 2.5)

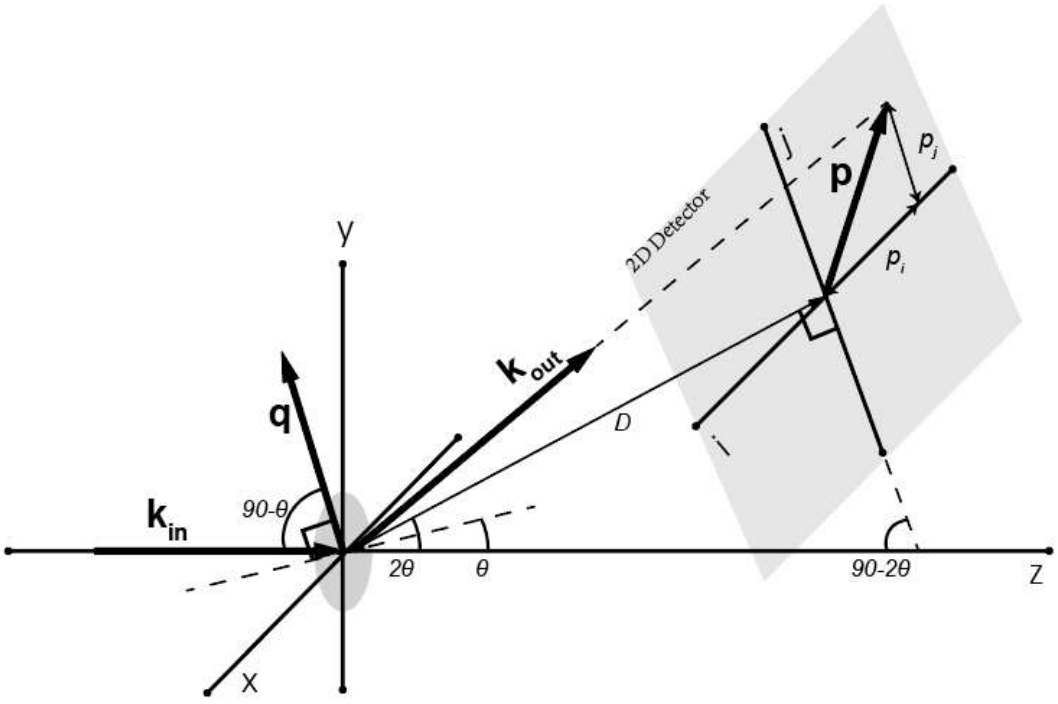


Figure 2.5
Geometrical illustration of the reconstruction method

The incident and scattered wavevectors could be described as

$$\vec{k}_{in} = \frac{2\pi}{\lambda}\vec{k}$$

$$\vec{k}_{out} = \frac{2\pi}{\lambda}\left(\frac{D\vec{d} + \vec{p}}{\sqrt{|D|^2 + |\vec{p}|^2}}\right)$$

in which λ is the wavelength and $\vec{k}, \vec{d}$ are the unit vectors of the incident beam and detector direction.

Then the wavevector scattering vector $\vec{q}$ could be described as

$$\vec{q} = \vec{k}_{out} - \vec{k}_{in} = \frac{2\pi}{\lambda}\left(\frac{D\vec{d} + \vec{p}}{\sqrt{|D|^2 + |\vec{p}|^2}} - \vec{k}\right) = \frac{2\pi}{\lambda}\left(\frac{D\vec{d} + p(I\vec{i} + J\vec{j})}{\sqrt{|D|^2 + p^2(I^2 + J^2)}} - \vec{k}\right)$$

Furthermore, the reciprocal cartesian coordinates based on the detector plane for pixel index (I, J) can be conducted as

$$\overrightarrow{q^x_{IJ}} = \vec{q} \cdot \vec{i} = \frac{2\pi}{\lambda}\left(\frac{pI}{\sqrt{|D|^2 + p^2(I^2 + J^2)}}\right)$$

$$\overrightarrow{q^y_{IJ}} = \vec{q} \cdot \vec{j} = \frac{2\pi}{\lambda}\left(\frac{pJ}{\sqrt{|D|^2 + p^2(I^2 + J^2)}} - \cos(2\theta + 90^o)\right)$$

$$\overrightarrow{q^z_{IJ}} = \vec{q} \cdot \vec{d} = \frac{2\pi}{\lambda}\left(\frac{D}{\sqrt{|D|^2 + p^2(I^2 + J^2)}} - \cos(2\theta)\right)$$

After interpolation (linear) the intensity of every pixel on the images with various theta angles, a 3D reciprocal space in the cartesian grid defined by $(\vec{i}, \vec{j}, \vec{d})$ is generated .

# ANALYSIS AND RESULTS

## *3D Reciprocal Space Observations*

As introduced before, all the $V_2O_3$ films are grown on sapphire substrates with various orientation: A-$(110)_R$, M-$(100)_R$, R-$(012)_R$. Although $V_2O_3$ has a similar structure as sapphire (both has a trigonal $R\bar{3}c$ symmetry), there is a significant difference in their lattice constants. For $V_2O_3$, the lattice parameters at room temperature are a=4.95Å and c=14.01Å with a c/a ratio of 2.83. However, for alpha alumina, the lattice parameters at room temperature are a=4.758Å and c=12.991Å with a c/a ratio of 2.73. The percentage of differences (referenced to $Al_2O_3$) is 4.04% for a, 7.84% for c and 3.66% for c/a ratio (compressive). Therefore, large biaxial strains are applied on these thin $V_2O_3$ films, which is also the most significant difference for the different oriented films.

To study the difference caused by the biaxial strains, the 2D projections of selected Bragg peak under various temperatures for the films grown on differently oriented substrates along two orthogonal directions are generated based on the 3D reciprocal space mapped. In the following parts, the observations and findings of A-, R- and M-oriented films will be introduced in order.

### *A-oriented Film*

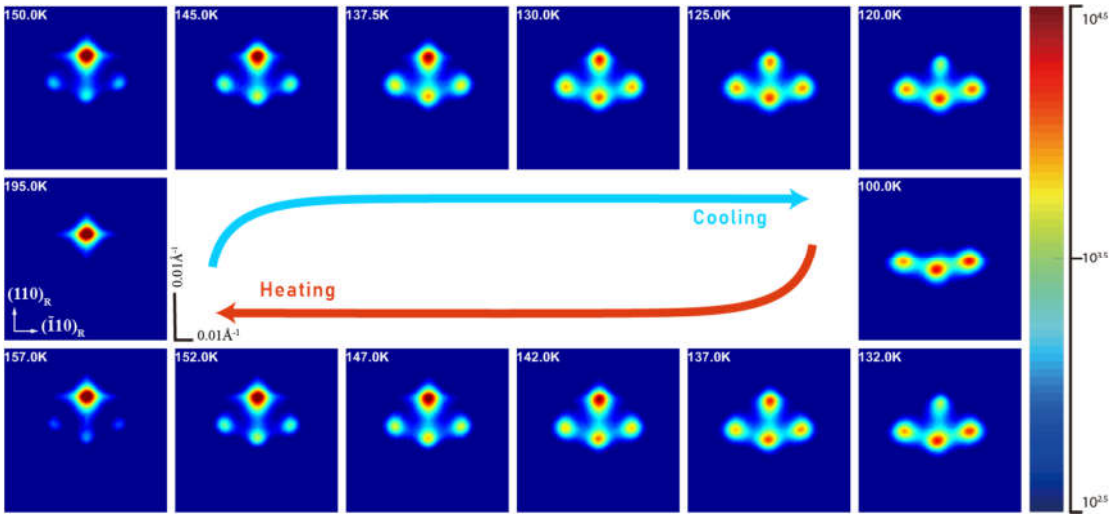


Figure 3.1

Reciprocal projections for A-(220) under various temperatures

The projection of the 3D-reciprocal space is along a direction parallel to $(001)_R$ plane. The vertical direction of the 2D projection patterns is parallel to $(110)_R$ plane and lateral direction to $(\bar{1}10)_R$ plane. Three low-temperature (LT) peaks are observed which all have a smaller q length than the high-temperature (HT) peak. Two symmetrical LT peaks on side have similar q length, and the one in center has a smaller q length. At lowest temperature(100K), the HT peak vanishes completely.

From the reciprocal space projections, the high-temperature peak $(220)_R$ transforms into three low-temperature peaks with similar intensity, which indicates all the three identical twinnings happen in the A-oriented film and the possibility of each twinning is close to the others. Two of low-temperature peaks are of the same q length, and the third one has a smaller q length. According to the transformations matrix introduced before, for rhombohedral $(220)_R$ plane, the corresponding three monoclinic planes are $(040)_M$, $(422)_M$ and $(4\bar{2}2)_M$ with an interplanar spacing of 1.251Å, 1.245Å and 1.245Å, respectively. Therefore, we index the diffraction pattern of $(040)_M$ plane as the central lower peak and the other two planes corresponding to the peaks on two sides. Other than the change of length of q, peak $(422)_M$ and peak $(4\bar{2}2)_M$ also symmetrically shift along

the direction perpendicular to the q direction, which makes all the peaks on a same plane in reciprocal space, as shown in Fig. 3.3(b). For brevity, the lateral projections are only shown for the measurements at 130K. Moreover, according to the shift length in reciprocal space, the tilt angle from $(220)_R$ to $(422)_M/(4\bar{2}2)_M$ is approximately 1.5 degree. The observations for $(110)_R$ and $(330)_R$ are similar to $(220)_R$.

In addition to the out-of-plane $(110)_R$ series peaks, we also measured the diffraction of $(012)_R$ planes, which has an interfacial angle of 42.4 degrees to the $(110)_R$.

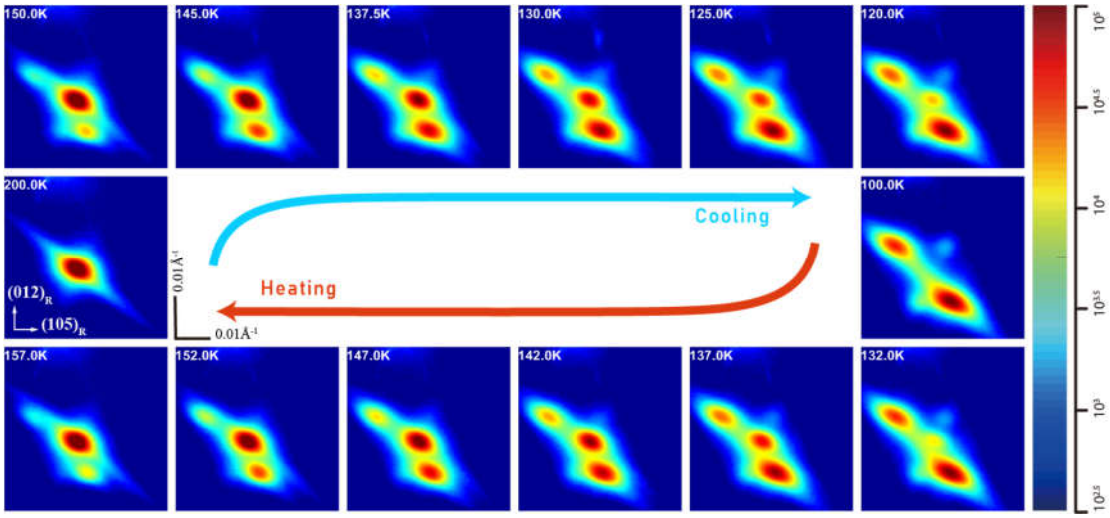


Figure 3.2
Reciprocal projections for A-(024) under various temperatures
The projection of the 3D-reciprocal space is along a direction parallel to $(\bar{1}20)_R$ plane. The vertical direction of the 2D projection patterns is parallel to $(012)_R$ plane and lateral direction to $(105)_R$ plane. Two LT peaks are observed. One has a larger q length and the other has a smaller q length than the HT peak. The intensity of the lower LT peak is much stronger than the higher LT peak.

In contrast to the three twins observed in $(220)_R$ peak, there are only two low-temperature peaks for $(024)_R$ peaks. For the $(024)_R$ planes, the possible monoclinic distortion planes are $(400)_M$, $(0\bar{2}2)_M$ and $(022)_M$ with an interplanar spacing of 3.612Å,

3.706Å and 3.706Å, respectively. Besides, the integral intensity for the lower peak is twice the intensity of the peak at the top. Therefore, it is evident that the lower peak results from the diffractions of $(0\bar{2}2)_M$ and $(022)_M$ planes together, while the higher peak comes from $(400)_M$ alone. Similar to the observations in $(220)_R$, all the shifted peak exists in one reciprocal plane, as shown in Fig.3.3(d). For the projections, the horizontal direction is $(105)_R$, and the vertical direction is $(024)_R$. By comparing the two reciprocal planes, we found they are perpendicular to each other.

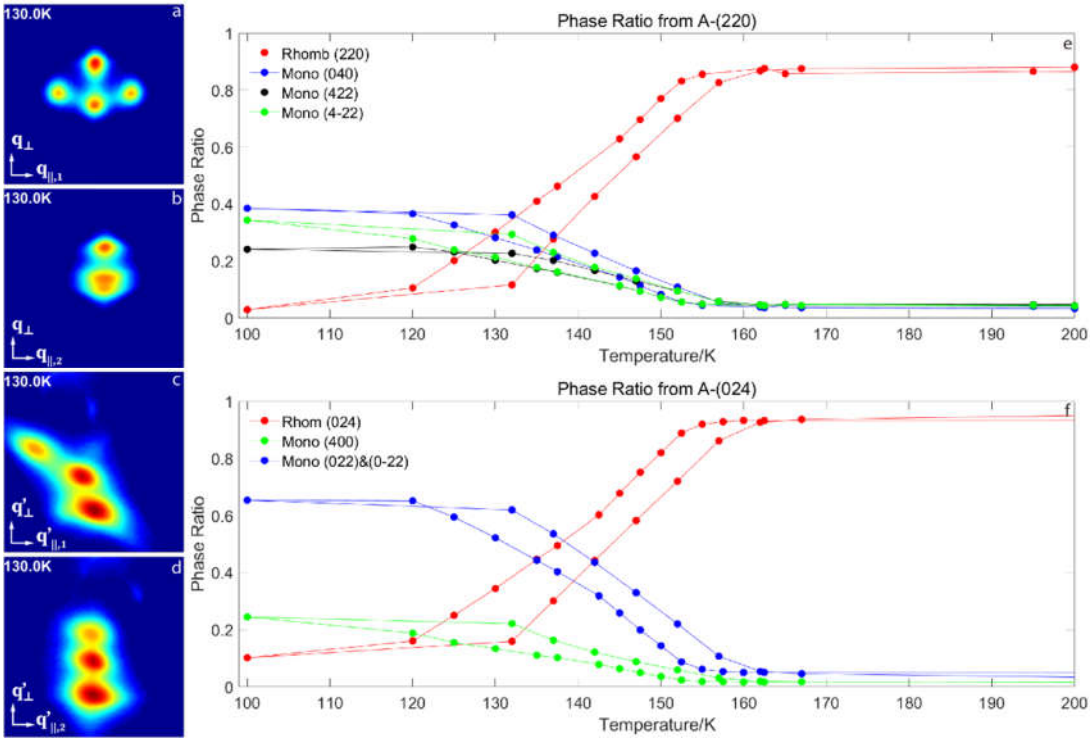


Figure 3.3

(a, b) The projections of A-(220) peak reciprocal space along orthogonal directions at 130K. $q_\perp$ is parallel to $(110)_R$ plane, $q_{\parallel,1}$ to $(\bar{1}10)_R$ and $q_{\parallel,2}$ to $(001)_R$. The shifting of the LT peaks is along $(\bar{1}10)_R$. (c, d) The projections of A-(024) peak reciprocal space along orthogonal directions at 130K. $q'_\perp$ is parallel to $(012)_R$ plane, $q'_{\parallel,1}$ to $(105)_R$ and $q'_{\parallel,2}$ to $(\bar{1}20)_R$. The shifting of the LT peaks is along $(105)_R$. (e, f) Phase ratio as function of temperature for A-(220) and A-(024) measurements. The phase ratios of the three LT twins in A-(220) are close to each other but not exactly identical. The intensity of the lower LT peak in A-(024) is much stronger than that of the higher LT peak, which indicates the lower LT peak may come from two of the three twins.

From the integral intensity of each peak, we can estimate the proportion of each phase presents in the film, as shown in Fig 3.3 (e, f). As expected, the characteristics of the proportion of the high-temperature phase from the measurements of different peaks are coincident with each other. As shown in the graph, the structural phase transition both starts at ~150K in the cooling process and ~120K in the heating process. The transformation temperature range is about 30K, and there is a ~5K temperature hysteresis between the cooling and heating process. For the measurement of $(024)_R$, we found the ratio of the integral intensities of the two low-temperature peaks is 2:1, as we discussed above. For the measurement of $(220)_R$, the integral intensities of the three low-temperature peaks are close to each other. However, there do exist differences within these three peaks. Besides, the differences are identical in the comparison of various temperature cycles. It indicates the presence of persistent underlying factors that affect the tendency of these three kinds of twinning, such as irregular local biaxial strain, which is beyond the scope of this study.

***R-oriented Film***

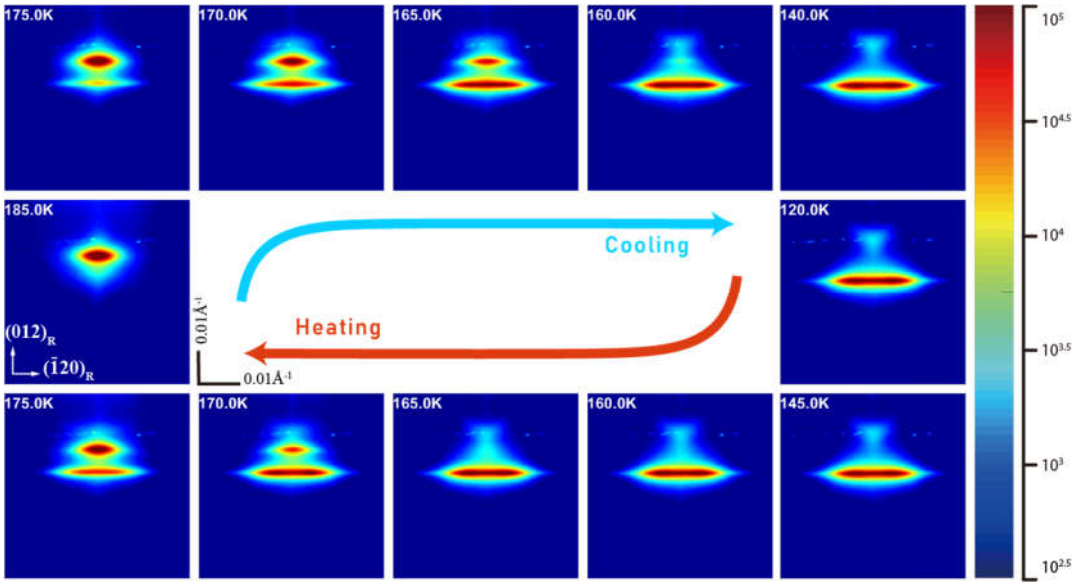


Figure 3.4
Reciprocal projections for R-(024) under various temperatures
The projection of the 3D-reciprocal space is along a direction parallel to $(105)_R$ plane. The vertical direction of the 2D projection patterns is parallel to $(012)_R$ plane and lateral direction to $(\bar{1}20)_R$ plane. Two LT peaks are observed, which have an identical lower q length than the HT peak. We also observed a weak LT peak with a larger q length than the HT peak.

Compared to the three twins observed in A-oriented film, there are only two obvious low-temperature peaks in the diffraction pattern of $(024)_R$ plane in the R-oriented film as shown in the graph above. Both low-temperature peaks have lower q length than the high-temperature peak. Therefore, the planar distance after distortion should be larger than the planar distance of $(024)_R$, which is 1.826Å. Therefore, compared to the planar distances for the possible distortion planes, the corresponding monoclinic planes should be $(0\bar{2}2)_M$ and $(022)_M$, which has a planar distance of 1.853Å. It is worth to notice there is still a nearly indistinguishable low-temperature peak at the top, which indicates the twinning of $(400)_M$ is greatly suppressed. Other than the number of twining, the

combined lower low-temperature peak in A-oriented film $(024)_R$ separate along $(\bar{1}20)_R$ direction in reciprocal space for R-oriented film with a link in-between, which could originate from the connection between the twins in the real structure.

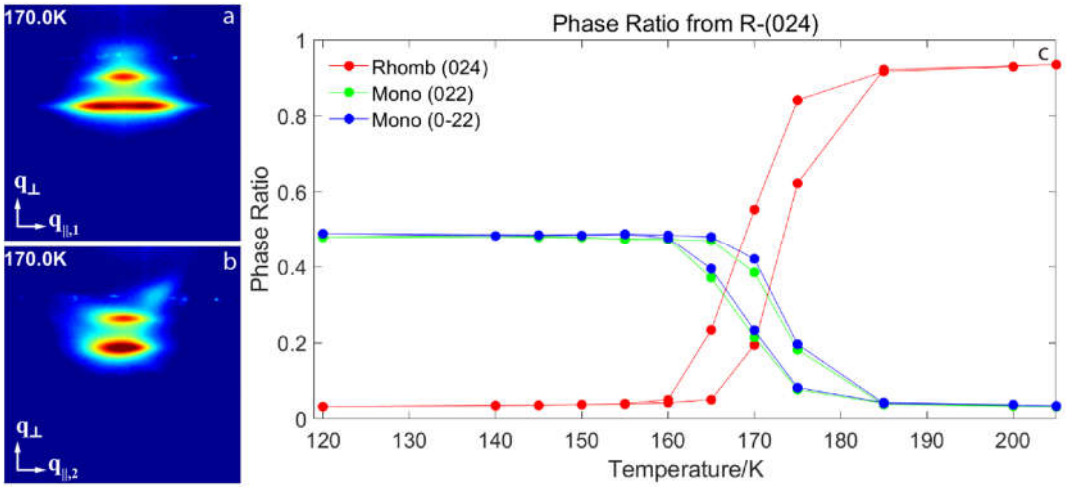


Figure 3.5

(a, b) The projections of R-(024) peak reciprocal space along orthogonal directions. $q_\perp$ is parallel to $(012)_R$, $q_{\parallel,1}$ to $(\bar{1}20)_R$ and $q_{\parallel,2}$ to $(105)_R$. The shifting of the LT peaks is along the $(\bar{1}20)_R$ direction. (c) Phase ratio vs Temperature for R-(024) measurements. The phase ratio of the two LT twins are identical to each other.

From the rhombohedral phase ratio in the film, it is shown that the SPT starts at ~175K in the cooling process and ~160K in the heating process. The transformation temperature range is about 15K for both processes, and there is a ~5K temperature hysteresis between the cooling and heating process. Besides, in contrast to A-oriented film, the possibility of these two kinds of twining are identical.

### *M-oriented Film*

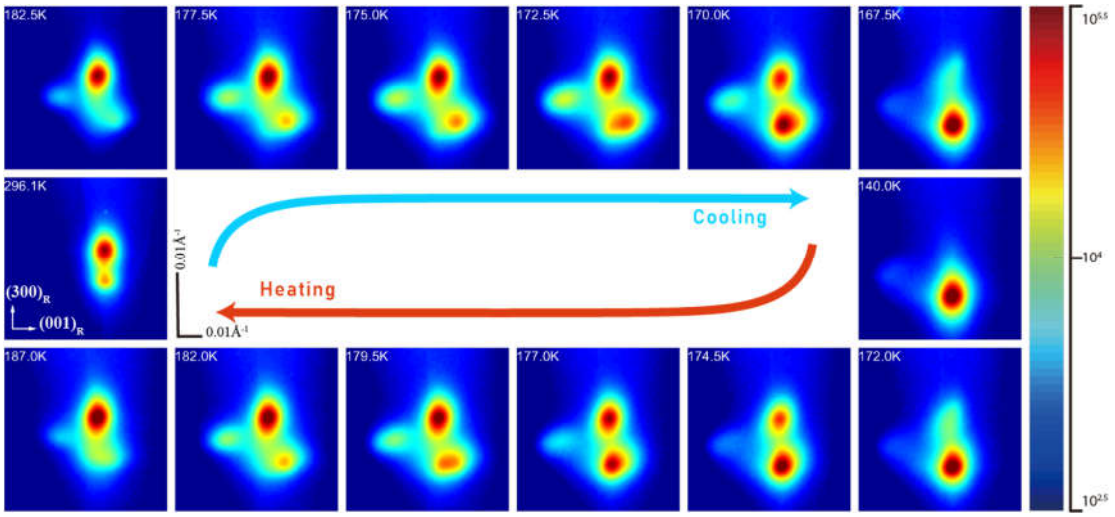


Figure 3.6

Reciprocal projections for M-(300) under various temperatures

The projection of the 3D-reciprocal space is along a direction parallel to $(\bar{1}20)_R$ plane. The vertical direction of the 2D projection patterns is parallel to $(100)_R$ plane and lateral direction to $(001)_R$ plane. At the lowest temperature, only one LT peak was observed, which has a smaller q length than the HT peak. Moreover, an intermediate peak was observed, which only presents in the middle of the transition and disappears at the highest and lowest temperatures. The q length of the intermediate peak is in between of the HT and LT peaks. In addition, a 'low-temperature' peak was observed at the highest temperature (296K), which relates to the gradually strained layer in the later discussion.

The diffraction pattern for the parallel-to-substrate plane of M-oriented film is more asymmetric than A- and R-oriented films discussed above. As shown in the Figure 3.6, surprisingly, at the highest temperature far above the SPT, there is already a 'low-temperature' peak, which has not been reported before. While cooling down to the SPT temperature, the diffraction result presents a duck-shaped pattern with the higher low-temperature peak as the "duck mouth". After further cooling, the "duck mouth" disappears and the other low-temperature peak turns into another low-temperature peak with identical q length, which has the same reciprocal orientation as the $(300)_R$ peak. The three possible kinds of twinning for $(300)_R$ planes are $(402)_M$, $(231)_M$ and $(2\bar{3}1)_M$

with an interplanar spacing of 1.435Å, 1.442Å and 1.442Å, respectively. Therefore, $(402)_M$ distortion should correspond to the "duck mouth" while $(231)_M$ and $(2\bar{3}1)_M$ corresponds to the two lower peaks. It is worth to notice that the first two distortion peaks all disappeared after further cooling and there is only one kind of twinning at the lowest temperature.

The horizontal direction of the projection $q_{\parallel}^{1}$ is $(001)_R$, and all the distortion peaks exist in one reciprocal plane (as shown in Fig. 3.9). Surprisingly, this is also exactly the reciprocal plane where the distortion of $(024)_R$ in A-oriented film happens.

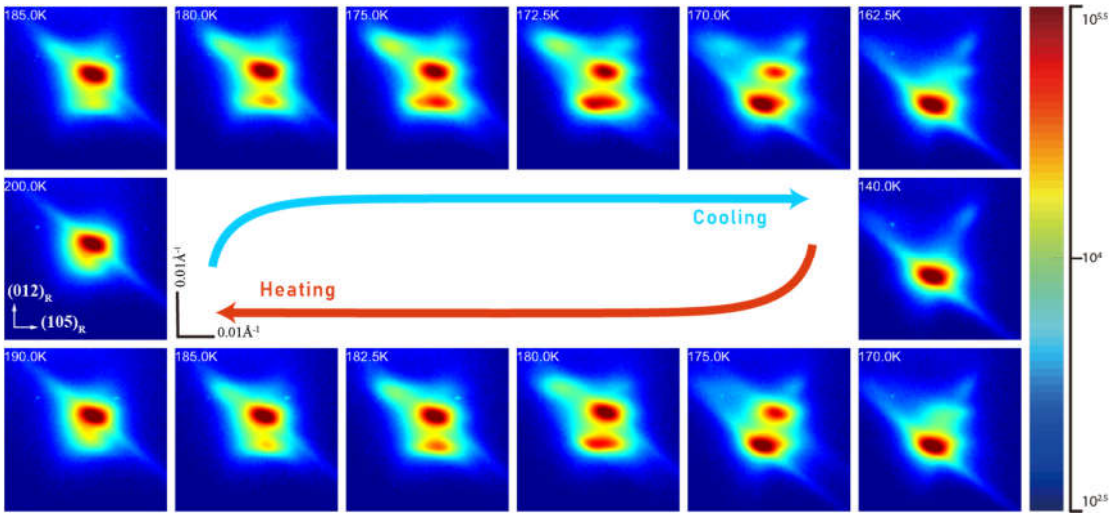


Figure 3.7

Reciprocal projections for M-(024) under various temperatures

The projection of the 3D-reciprocal space is along a direction parallel to $(\bar{1}20)_R$ plane. The vertical direction of the 2D projection patterns is parallel to $(012)_R$ plane and lateral direction to $(105)_R$ plane. Similar to the observation in M-(300), only one LT peak was observed at the lowest temperature, and an intermediate peak was observed. The q length of the intermediate peak is larger than the HT peak and the q length of the LT peak is smaller than the HT peak.

Similar to the observation in $(300)_R$ peak, the intermediate phases are also observed in the diffraction of $(024)_R$ plane in M-oriented film, and there is only one diffraction peak

at the lowest temperature. As shown above, the low-temperature peak at the top appears in the cooling process and disappear after further cooling. Moreover, the lower low-temperature peak shifts in $q_{\|,1}$ direction as expected. As discussed before, the low-temperature peak at the top corresponds to the $(400)_M$ distortion phase, and the two lower peaks correspond to$(0\bar{2}2)_M$ and $(022)_M$.

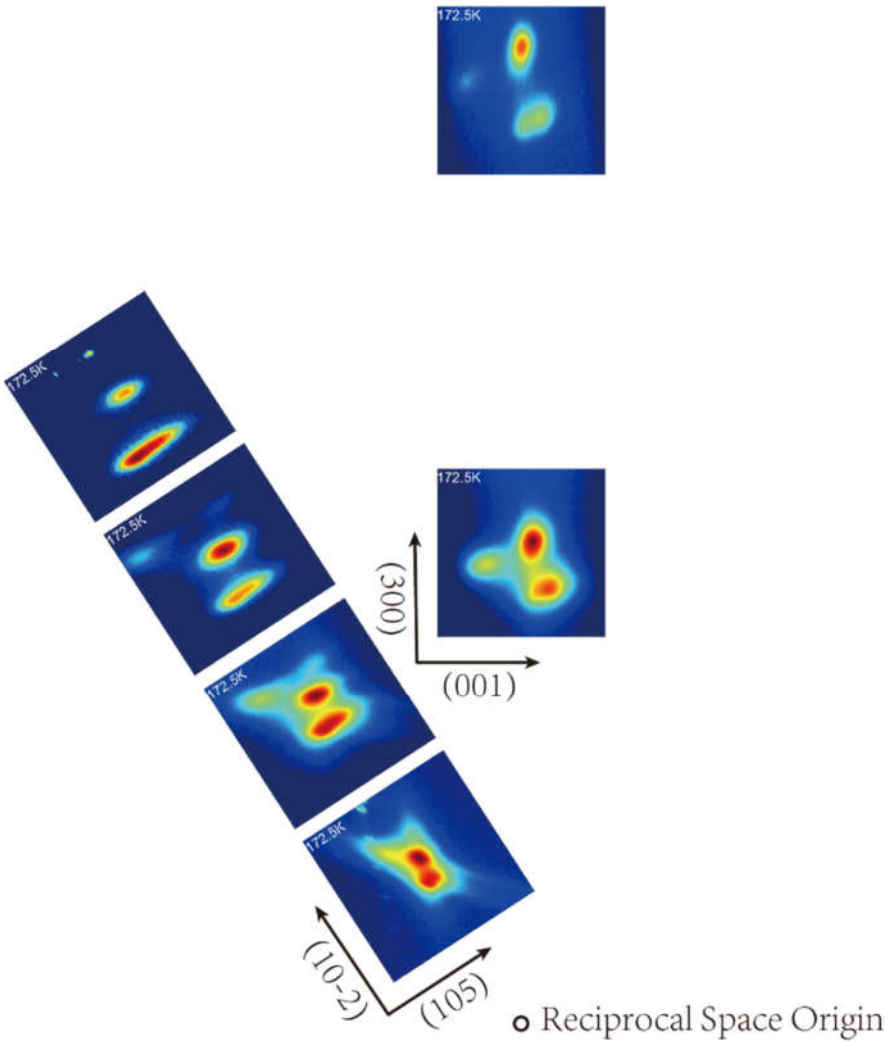


Figure 3.8
Reciprocal space of M-oriented film
The projection of the 3D-reciprocal space is along a direction parallel to $(\bar{1}20)_R$ plane. And the projections of various peaks are arranged in their corresponding positions and orientations in the reciprocal space.

The horizontal direction for the projection above is $(105)_R$. Therefore, the reciprocal peak shift planes of $(300)_R$ series peaks and $(012)_R$ series peaks are identical. Meanwhile, the vertical directions of the projections have a 33-degree difference. The diffraction peaks on the reciprocal shift plane could be combined as Fig. 3.8. In the graph, as a result of the three-fold symmetry, the $(10\bar{2})_R$ is the identical lattice plane to $(012)_R$.

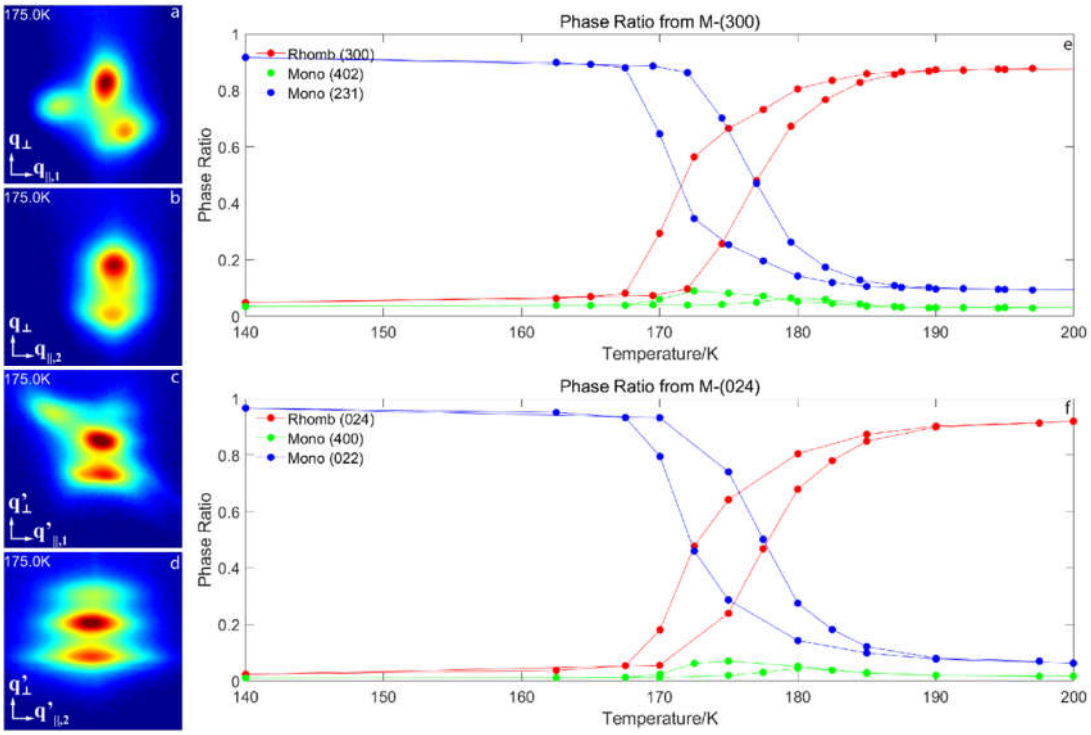


Figure 3.9

(a, b) The projections of M-(300) peak reciprocal space along orthogonal directions at 175K. $q_\perp$ is parallel to $(100)_R$, $q_{\parallel,1}$ to $(001)_R$ and $q_{\parallel,2}$ to $(\bar{1}20)_R$. The shifting of the LT peaks is along the $(100)_R$ direction. (c, d) The projections of M-(024) peak reciprocal space along orthogonal directions at 175K. $q'_\perp$ is parallel to $(012)_R$, $q'_{\parallel,1}$ to $(105)_R$ and $q'_{\parallel,2}$ to $(\bar{1}20)_R$. The shifting of the LT peaks is along the $(105)_R$ direction. (e, f) Phase ratio as a function of temperature for M-(300) and M-(024) measurements. The phase ratios calculated from the two measurements are identical to each other.

As shown above, the phase ratio of the rhombohedral phase and the intermediate low-temperature phase calculated from $(024)_R$ peak and $(300)_R$ peak is consistent with each other as expected. The SPT starts at ~180K in the cooling process and ~172K in the

heating process. The transformation temperature range is about 12K for both processes, and there is a ~5K temperature hysteresis between the cooling and heating process. Besides, because the phase ratio variation trend of the intermediate phase is identical for both measurements, it is reasonable to consider the two intermediate diffraction peak comes from the same distortion structure, which represents as the $(402)_M$ and $(400)_M$ distortion in the two measurements, respectively. It is worth to notice that there exists a huge difference between the amounts of intermediate phase in cooling and heating processes. In the cooling process, the maximum of the intermediate phase ratio is ~1.5 times larger than that in the heating process.

***Summary***

For the simplicity of comparison, the prominent characteristics of the observations are summarized in the table below.

| Substrates Orientation | SPT Temp. During Cooling | SPT Duration | Temperature Hysteresis | Twinning Numbers |
|---|---|---|---|---|
| A | 150K | 30K | 5K | 3 |
| R | 175K | 15K | 5K | 2 |
| M | 180K | 12K | 5K | first 2, then 1 |

Table 3.1
SPT SUMMARY (The start and end of SPT is calculated from the 0.9 point and 0.1 point of the rhombohedral phase during the cooling process)

From the table, we can tell that the SPT of A-oriented films requires a lower temperature and a larger temperature range to complete the transformation than the other two films. Moreover, it is also the only films that all three twins happen, and the one with the transition temperature most close to bulk $V_2O_3$. However, for R- and M-oriented films, there only presents two or one twins in the films, and they perform the structural transition at a higher temperature than A-oriented film. Therefore, it is reasonable to infer that, in R- and M-oriented films, the biaxial strain in these films is preferable to one or two specific kinds of twinning, which lower the energy barrier to start the SPT and greatly suppress the other possible kinds of twinning at the same time.

Moreover, as the thickness of the sapphire substrate is far larger than the $V_2O_3$ film on top, and the modification to the substrate is negligible in the deposition process, it's reasonable to assume the lattice parameter of the sapphire substrate remains the same after deposition, which means a few percent of biaxial strain are introduced into the $V_2O_3$ films through epitaxial growth. In general, this large biaxial strain will easily break the bulk crystalline materials. However, in the process of epitaxial growth, crystallographic defects (dislocation) are included to compensate for the difference between substrate and deposited films. (As shown in Figure 3.10) The defects are ubiquitous at the interface between substrate and films where the maximum of lattice difference occurs. However, with the increase of the distance from the substrate, the film's biaxial strain is gradually relaxed, which will cause a significant reduction of the dislocation density. At the point above tens of nanometers away from the substrate, typically the lattice is relaxed fully relaxed. Therefore, for the films grown on various oriented sapphire substrates, the only difference exists in the biaxial strains in the layer next to the film-substrate interface. For the film above this layer, they should be composed of essentially identical fully relaxed $V_2O_3$.

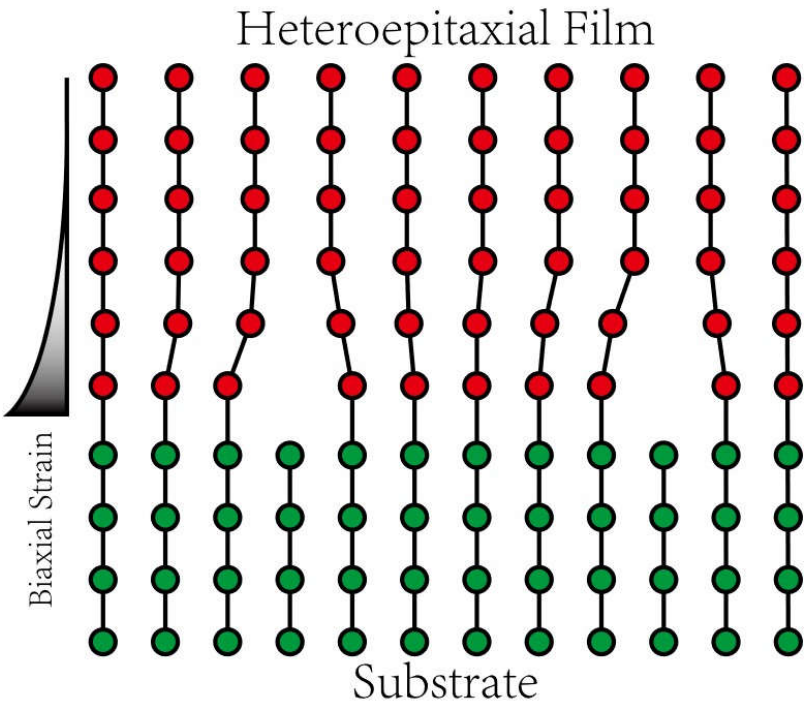


Figure 3.10
Illustration of film-substrate interface

Though the underlying factors for our observation could be complicated and difficult to be resolved only with our measurements, one possible origin for the difference in the twinning dynamics is the biaxial strain due to differential thermal contraction. It can be assumed that the films are completely relaxed at the growth temperature (800℃) because of the high thickness (300nm) of the films. And as a result of the thermal expansion coefficient of $V_2O_3$ is smaller than $Al_2O_3$, during cooling towards the transition temperature (150 K), the substrate will clamp the film and induce a biaxial compressive strain. This strain is applied along the substrate surface, meaning different crystallographic planes in the $V_2O_3$ crystal. The biaxial strain may facilitate the formation of some specific twins in differently oriented films, which results in the different number of twins observed in different films.

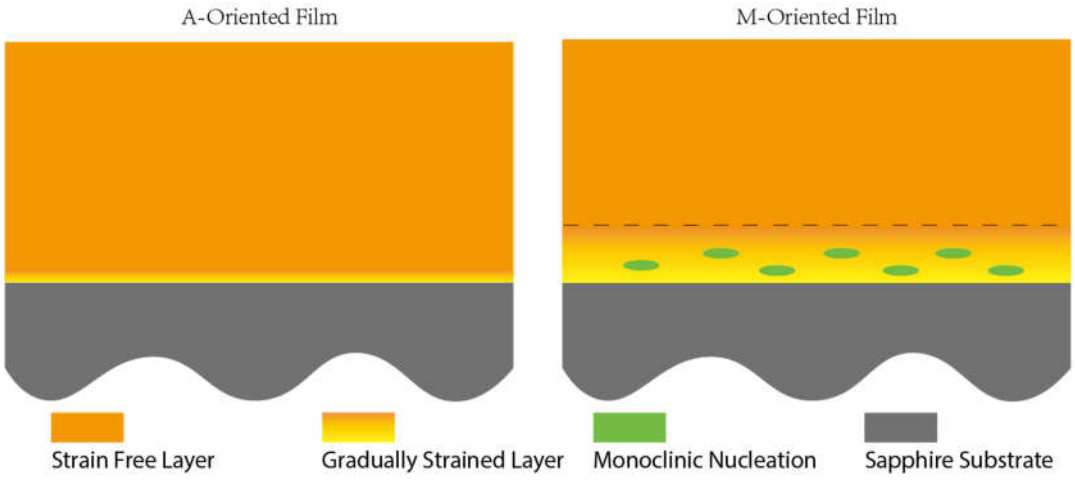


Figure 3.11
Illustration of the gradually strained layer in A- and M-oriented films.

In addition to the different orientation and magnitude of the biaxial strain in variously oriented films, another important possible factor comes from the different thicknesses of films that the biaxial strains have effects on. For example, a 'low-temperature' peak was observed at the highest temperature with a shorter q length as shown in Fig. 3.6. We assume this peak may come from the gradually strained layer in the $V_2O_3$ film next to the substrate (as shown in Fig. 3.11). Moreover, we think the biaxial strain within this layer may facilitate the formation of some specific monoclinic distortions in M-oriented film, which will greatly increase the transition temperature as we observed experimentally. Furthermore, the nucleation in the gradually strained layer could also significantly accelerate the formation of the specific monoclinic phase and suppress the formation of the other possible distortions. Consistent with our assumption, the 'low-temperature' peak of M-$(300)_R$ disappears first during the initial SPT then the intensity

of the $(300)_R$ peak starts to decrease, which indicates the gradually strained layer transits into monoclinic phase before the relaxed rhombohedral phase.

Under our assumption, the A-oriented film should have the thinnest gradually strained layer. In other words, most of the A-oriented film is composed of relaxed $V_2O_3$, which makes all three possible twins form and the film transits at the similar temperature as bulk $V_2O_3$ do.

However, the structure of the gradually strained layer is mysterious and the reason why the gradually strained layer thickness is different for various oriented film is still unclear. One possible explanation is the different vanadium atoms density of the three lattice planes. According to calculation, the vanadium atom densities for $(110)_R$, $(012)_R$ and $(300)_R$ are $0.100/Å^2$, $0.074/Å^2$ and $0.058/Å^2$, respectively. Besides, it is well known that the lattice parameters of the sapphire substrate are much smaller than vanadium sesquioxide (4.04% for a and 7.84% for c). As we discussed before, within the interface between the films and substrates, there should be biaxial compressive stress provided to the films by the sapphire substrate. Our assumption is, for the plane with smaller atoms density (larger interatom spacing), the vanadium atoms tend to compensate the lattice parameter difference by connecting to the adjacent Al atom and gradually release the biaxial strain during the further growth. But for the plane with larger atoms density, the small interatom spacing limits the ability of in-plane shifting of vanadium atoms. Therefore, it prefers to compensate for the differences by introducing defects, which could dramatically release the biaxial strain. In other words, there are more lattice

defects and thinner strained layer in the plane with larger atom density. Furthermore, as the existence of the large compressive biaxial strain, the lattice distance of the strained layer should be larger than that of the relaxed region. In this way, the Bragg peak of the gradually strained layer should have a shorter q than the relaxed film, which is consistent with our experimental observations in M-oriented film.

## *Microstrain Analysis using Williamson-Hall Method*

Microstrain is a factor that reflects the variance of strain states in a material, which should be carefully distinguished from strain: the larger the microstrain, the bigger the strain gradients. Therefore, the microstrain may be negligible in a highly strained material as long as the strain state is identical everywhere.

As discussed in chapter one, the broadening of X-ray diffraction peaks along the q direction could be caused by the microstrain and finite coherently scattering domain size normal to the lattice planes measured. With the Williamson-Hall method, we successfully separated these two broadening factors and analyzed the microstrain states under various temperature, which provided us much valuable structural information about the vanadium sesquioxide films during its SPT.

### *A-oriented film*

For $(110)_R$ series peaks of A-oriented film, the peak shapes coincide with Lorentzian function. Therefore, the integral peak width should be plotted linearly with q length in the Williamson-Hall plot, as shown in Fig. 3.12(a) (only showed a few plots of the high-temperature peak for clarity). Furthermore, according to the gradient of the fitted plot, the corresponding microstrain could be retrieved for the phase represented by each peak.

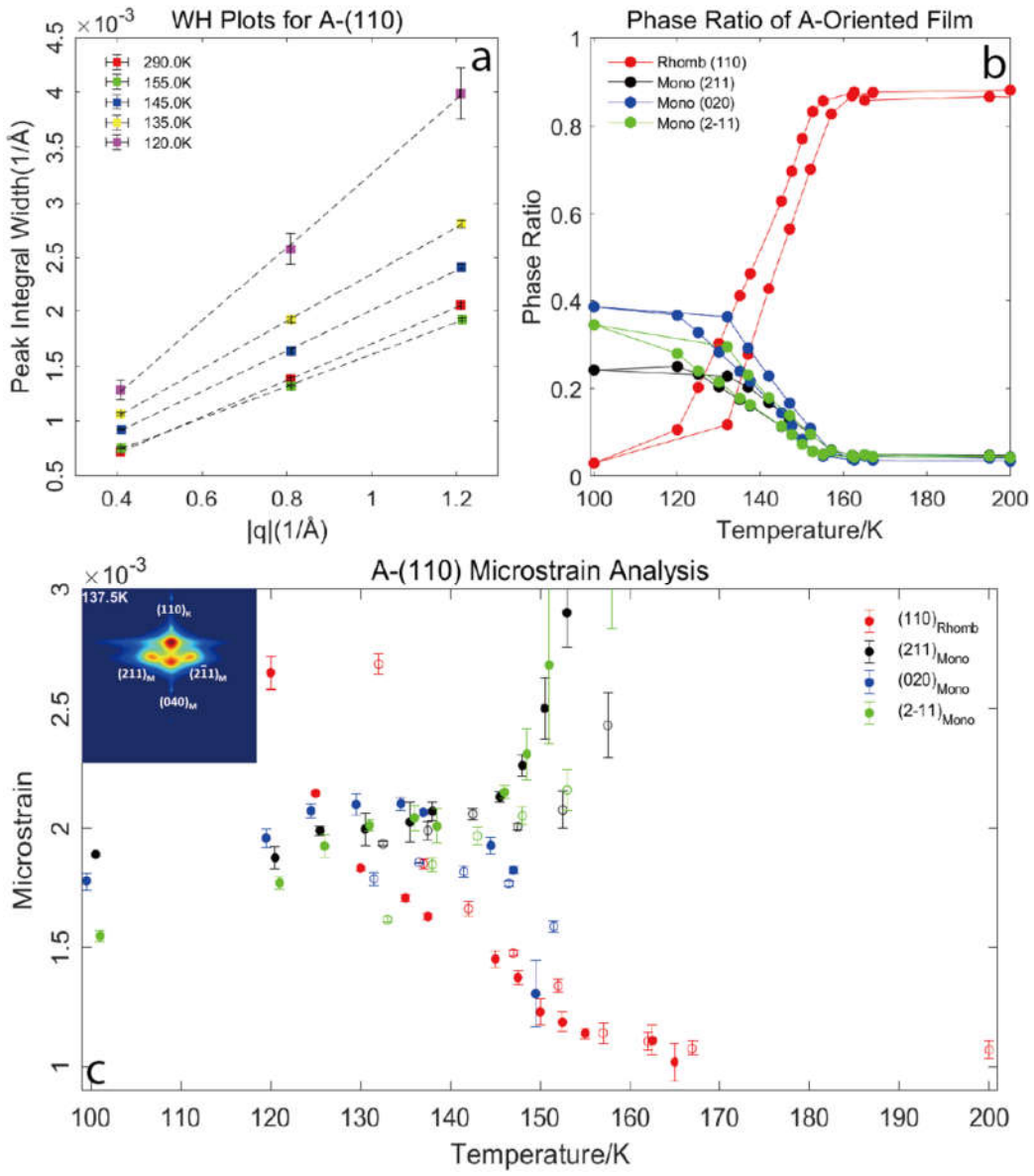


Figure 3.12

(a)Williamson-Hall plots for A-$(110)_R$ rhombohedral phase. (b) Ratios of various phases as a function of temperature. (c)A-(110) microstrain of various phases vs temperature. The solid dots come from cooling process while the hollow ones for heating process. In the cooling process, the microstrain of the $(110)_R$ and $(020)_M$ increase, and the microstrain of $(211)_M$ and $(2\bar{1}1)_M$ decrease. Moreover, hysteresis was observed clearly in the microstrain evolution of all the phases.

As shown in Fig. 3.12(c), the microstrain of phases change significantly during the SPT, indicating large strain gradients presumably at the interfaces between different structures present. For the high-temperature rhombohedral phase, it is easier to

understand why its microstrain increases during the cooling process. At high temperature, though the film may be strained as a result of the heteroepitaxial growth, the strain states are consistent everywhere. When the transition happens, it introduces a lot of Rhomb-Mono phase boundaries. Because the mismatch of lattice between Rhombohedral and Monoclinic structures, the strain of the portion close to the boundary is greatly different with the portion in the center of the domain (as shown in Fig. 3.13), which will directly increase the microstrain of the phase.

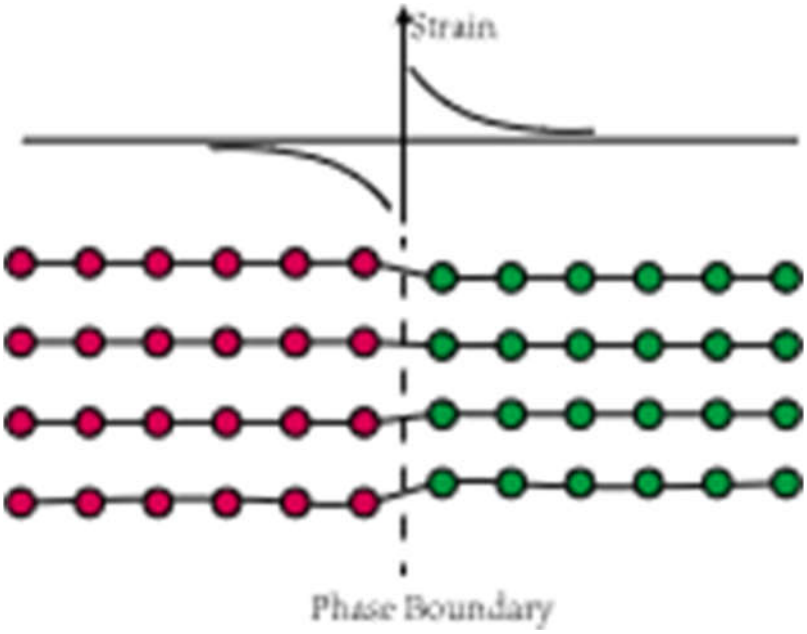


Figure 3.13
Illustration of strain variation as a function of distance from phase boundary

With more and more monoclinic domains appearing in the film, the microstrain of the rhombohedral phase increases with the volume of interfaces. However, the total volume of the interface is not the only factor that affects the microstrain. For example, the microstrain of a single domain is much smaller than an aggregation of small domains which has the same interfacial area. In other words, the microstrain of a phase depends

on the volume of its interface as well as its total volume, which could be compared to the specific surface area. At the end of the SPT, the total amount of phase interface is reduced. But as a result of the little total rhombohedral volume, the microstrain still keeps growing. The same explanation could also be applied to understand the decreasing of the microstrain in the $(211)_M$ and $(2\bar{1}1)_M$ distortion phase. And we can also infer that the isotropic growth of the $(211)_M$ and $(2\bar{1}1)_M$ distortion phase, which pushes the phase interfaces isotropically during growth. However, for the $(020)_M$ distortion phase, in the cooling process, although its total volume greatly increased according to the phase ratio, the microstrain of it surprisingly increases first then decreases. Therefore, we think that the growth of the phase interface greatly exceeds the growth of its total volume in the initial SPT. To reach this goal, it is reasonable to infer the $(020)_M$ distortion phase grows in a planar anisotropic mode.

Besides, it is worth to notice that the microstrain of $(020)_M$ distortion phase starts to decrease as soon as the high-temperature rhombohedral phase vanished. From the phase ratio, we can conclude that the amount of $(020)_M$ distortion phase is approximately constant at that temperature, one possible explanation to the variation of microstrain is that most of the interfaces are between the $(020)_M$ distortion phase and the rhombohedral phase. Once the rhombohedral phase disappears, the interface volume greatly decreased, which makes the strain of the $(020)_M$ distortion phase more uniform.

***R-oriented film***

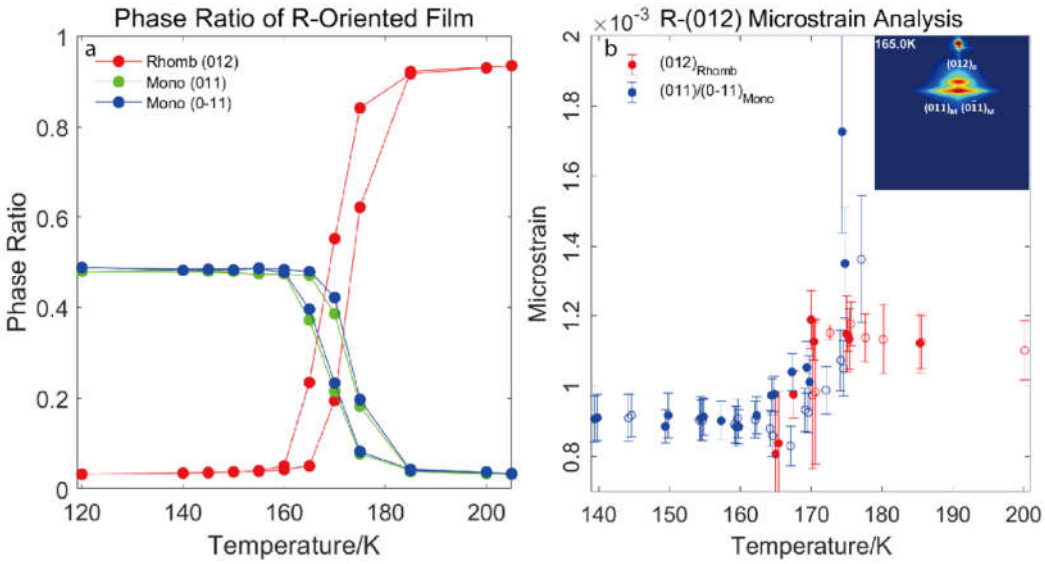


Figure 3.14
(a)Phase ratio vs temperature based on R-(024) (b)R-(012) microstrain of phases vs temperature. The solid dots represent for cooling process while the hollow ones for heating process. In the cooling process, the microstrain of the rhombohedral phase and monoclinic both decrease during the SPT.

In the R-oriented film, we analyzed its microstrain based on its out-of-plane $(012)_R$ series peak. As shown in the graph above, in the cooling process, the microstrain of the rhombohedral and monoclinic phase keep decreasing during the SPT. And in the temperature range out of the SPT, the microstrain of both phases stays constant. As discussed before, the microstrain decrease of the monoclinic phase is easy to understand, which indicates its decreased specific surface area and isotropic growth configuration. However, if the same assumption holds for the rhombohedral phase, its microstrain should increase during the SPT instead of decreasing. In contrast to the observation in the microstrain analysis of A-oriented film, the initial microstrain of the rhombohedral phase is larger than that of the monoclinic phase at the lowest temperature. At the lowest temperature, there are two distortion phases for R-oriented film, which will likely create

be separated by interfaces. Therefore, the microstrain of the pure rhombohedral phase should be smaller than that of pure monoclinic phase, as shown in the A-oriented film. Besides, it's worth to notice that the microstrain of the rhombohedral phase at 200K is larger for R-oriented film (1.10e-3) than that for A-oriented film (1.07e-3). The possible reason could be the thicker strained layer next to the interface, as discussed above. The strained layer for R-oriented film could be thicker than that of the A-oriented film as a result of different atom density in the planes. In the thicker strained layer, the lattice mismatch between substrate and film are released gradually, which introduce a large variance of strain into the pure rhombohedral phase and directly increase the microstrain. Furthermore, as discussed, the strained layer has a great probability of transforming earlier than the top strain-free film. Therefore, when the SPT happens, this layer will disappear first and decrease the variance of strain at the same time.

***M-oriented film***

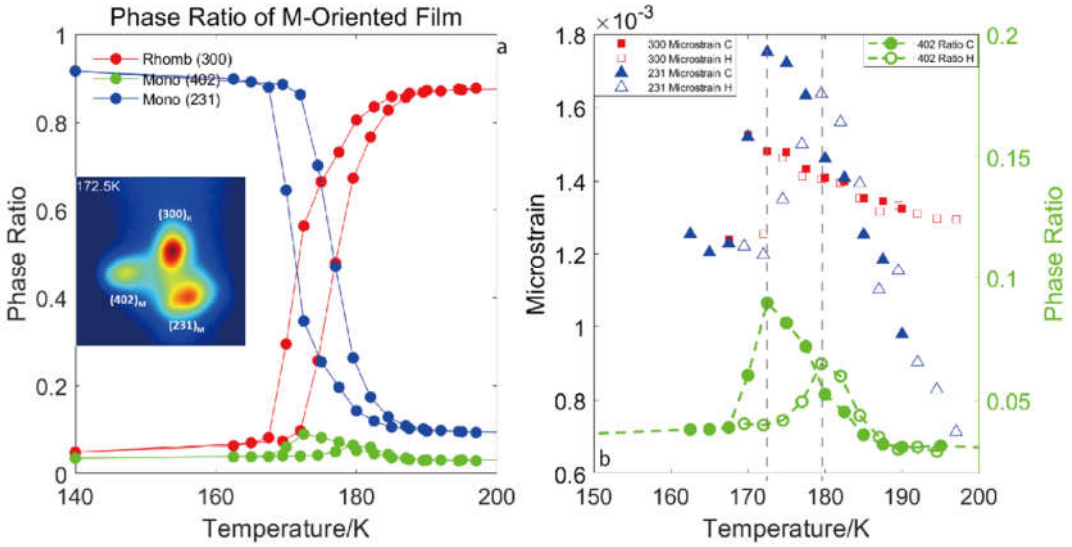


Figure 3.15
(a)Phase ratio vs temperature based on M-(300) (b)M-(300) microstrain of phases vs temperature. The solid dots represent for cooling process while the hollow ones for heating process. In the cooling process, the microstrain of the rhombohedral phase and monoclinic phase both increase first then decrease. Moreover, the phase ratio of the intermediate phase $(402)_{Mono}$ is correlated to the microstrain of $(231)_{Mono}$ phase.

In the M-oriented film, the existence of the intermediate distortion phase makes the microstrain result more intriguing than A and R. As shown in in Fig. 3.15(b), in the cooling process, the microstrain of both $(300)_R$ and $(231)_M$ increases first and then decreases, which is different to the monotonic variation of microstrain observed in A and M. And as shown in Fig. 3.15(a), the phase amount of $(300)_R$ consistently decreases and $(231)_M$ consistently increases during the cooling as expected. Combining these two observations, we can conclude that the interface of the monoclinic phase was greatly increased in the initial cooling process. The possible reason could come from the strained layer next to the substrate discussed above. At the start of the SPT, the monoclinic phase nucleates in the strained layer first, which increases the its microstrain.

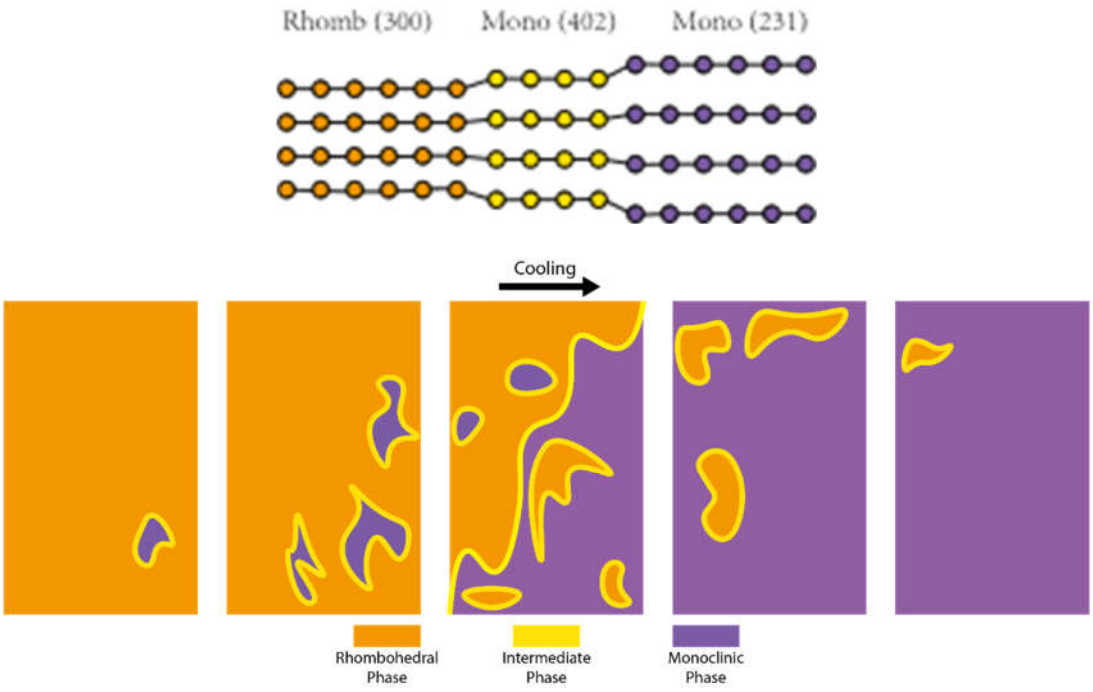


Figure 3.16
Schematic illustration of phase transition

Besides, we also found the microstrain of the $(231)_M$ distortion phase is surprisingly coincident with the total $(402)_M$ phase amount present, which strongly indicates the $(402)_M$ phase is served as the surface phase interface of $(231)_M$ phase. In other words, the amount of the $(402)_M$ phase directly correlates to the volume of interfaces of the $(231)_M$ phase. And it is worth noticing that the intermediate phase disappears as soon as the rhombohedral phase vanishes. It indicates the intermediate phase not only serves as the surface of the $(231)_M$ phase but also for the $(300)_R$ phase, namely, the interface of these two phases. As shown in Fig. 3.16, from the diffraction pattern of the M-$(300)_R$ peak, we found the lattice distance of the intermediate phase ($(402)_M$) is larger than the rhombohedral phase ($(300)_R$) and smaller than the monoclinic phase ($(231)_M$). Moreover, at the highest and lowest temperature, the SPT just starts and the phase boundary is little.

While in the middle temperature, as a result of the phases percolation, the interfacial volume is greatly increased. Therefore, in the Fig.3.15(a), the phase ratio of the intermediate phase increases first then decreases, which is also directly reflected in the microstrain analysis.

***Summary***

| Substrate Orientation | Microstrain at ~200K | Microstrain at lowest T |
|---|---|---|
| A | 1.07e-3 | 1.74e-3(100K) |
| R | 1.10e-3 | 0.91e-3(140K) |
| M | 1.32e-3 | 1.28e-3(140K) |

Table 3.2

From our previous assumption, at the highest temperature, the thickness of the gradually strained layer should decrease as M-, R- and A-oriented films. Moreover, as we discussed, the thicker the gradually strained layer, the larger microstrain (uniformity) should present in the film. Our assumption is proved by the comparison of the microstrain at 200K for various oriented films as shown in table 3.2, which decreases as M-, R- and A-oriented films.

Furthermore, the microstrains of the various oriented films at the lowest temperature also agree with the twins we observed. In A-oriented film, all three twins present and there are two different lattice spacings along the out-of-plane direction (as shown in the inset of Fig, 3.12 c). Therefore, there should be a lot of interface between the different-lattice-spacing phases, which will dramatically increase its microstrain in the pure monoclinic state. For the R-oriented film, (as shown in the inset of Fig, 3.14 b), from the diffraction pattern, we found the lattice spacing of the two twins are identical. Therefore, although two twins present, but the microstrain introduced by the interface between same-lattice-spacing phases is negligible, which is coincident with our

observation. However, for the M-oriented film, although we only observed one twin at the lowest temperature, the microstrain of it is larger than R-oriented film at lowest temperature. One possible reason for that is the remnant of the intermediate phase. As shown in the Fig. 3.17, we compared the diffraction patterns of $(300)_R$ at 197K and 140K. We found there is still a little intermediate phase exists at 140K. Therefore, it's reasonable to conclude that the phase boundary doesn't disappear entirely after the SPT, which will result in the large microstrain in the M-oriented film.

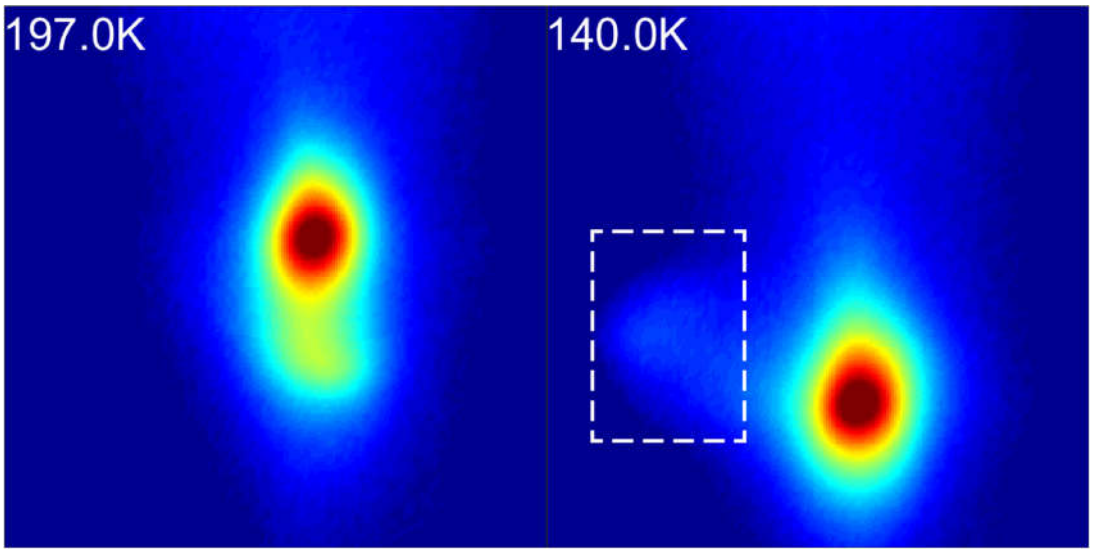


Figure 3.17
Comparison of the reciprocal projections at highest and lowest temperature for M-(300)
A weak peak was observed at the position of the intermediate peak at the lowest temperature (140K), which indicates the remnant of the intermediate phase.

# CONCLUSIONS

We performed X-ray diffraction on $V_2O_3$ thin films grown on various oriented sapphire substrates. From the reconstructed 3D reciprocal space, we found the number of twins present in the films changes as a function of the substrate orientation. Besides, we found the number of twins anticorrelates with the MIT temperature: lowest temperature for three twins, intermediate temperature for two twins and highest temperature for one twin. And the substrate orientation also affects the duration of the structural phase transition. Plausible models based on different biaxial strains are raised to explain difference in twinning.

We also performed the microstrain analysis using Williamson-Hall method. In A-oriented film, we found the microstrain state of one twin is different from the others, which imply the different morphology of various twins. In M-oriented film, an intermediate phase was discovered. Moreover, we found the amount of the intermediate phase present in the M-oriented film is correlated to the microstrain state of the rhombohedral phase and monoclinic phase, which indicates it could serve as the phase boundary between these two phases.

# PERSPECTIVE

The X-ray energy used in this study is 14.5KeV. And the detector motor 2theta range is 0~75 degree. Therefore, only limited Bragg peaks are accessible in our measurements. In the future, we could study the film with X-ray of higher energy. In this way, more peaks are available for each series of peak. And the Williamson-Hall plot could be fitted with more points, which will greatly increase the accuracy of the microstrain analysis.

Besides, as introduced in this study, an intermediate phase was discovered in the M-oriented film. And it is promising to be the interface between the rhombohedral and monoclinic phase. Therefore, to verify this assumption, a study of the intermediate phase spatial distribution and the spontaneous formation of spatial patterns amidst insulator–metal phase coexistence on the meso- and nanoscales is in urgent need. Moreover, as a result of the depth-dependent property of the films, the optimal characterization method should have a relatively long penetrate depth, such as hard X-ray nano probe.

Furthermore, as the ramp-reversal memory property was reported in this film(reference), the intermediate phase could be very likely the structural ‘scar’ that left by the phase boundary, which has a significant effect on the film’s electrical transport properties. Therefore, an in-situ study should be carried out to investigate the correlation of the intermediate phase and the ramp-reversal memory phenomena in the films.

# REFERENCES


1. D. B. McWhan & Remeika, J. P. Metal-Insulator Transition in (V1-xCrx)2O3. *Phys. Rev. B* **2**, (1970).
2. Dernier, P. D. & Marezio, M. Crystal structure of the low-temperature antiferromagnetic phase of V2O3. *Phys. Rev. B* **2**, 3771–3776 (1970).
3. Mott, N. F. The basis of the electron theory of metals, with special reference to the transition metals. *Proc. Phys. Soc. Sect. A* **62**, 416–422 (1949).
4. McWhan, D. B., Menth, A., Remeika, J. P., Brinkman, W. F. & Rice, T. M. Metal-insulator transitions in pure and doped V2O3. *Phys. Rev. B* **7**, 1920–1931 (1973).
5. McWhan, D. B., Rice, T. M. & Remeika, J. P. Mott transition in Cr-Doped V2O3. *Phys. Rev. Lett.* **23**, 1384–1387 (1969).
6. Pfuner, F. *et al.* The metal-insulator transition in V2O3(0001) thin films: Surface termination effects. *J. Phys. Condens. Matter* **17**, 4035–4047 (2005).
7. Yonezawa, S., Muraoka, Y., Ueda, Y. & Hiroi, Z. Epitaxial strain effects on the metal-insulator transition in V 2O3 thin films. *Solid State Commun.* **129**, 245–248 (2004).
8. Luo, Q., Guo, Q. & Wang, E. G. Thickness-dependent metal–insulator transition in V2O3 ultrathin films. *Appl. Phys. Lett.* **84**, 2337–2339 (2004).
9. Allimi, B. S. *et al.* Resistivity of V2 O3 thin films deposited on a -plane (110) and c -plane (001) sapphire by pulsed laser deposition. *Appl. Phys. Lett.* **92**, 2–5 (2008).
10. McLeod, A. S. *et al.* Nanotextured phase coexistence in the correlated insulator

v 2 O 3. *Nat. Phys.* **13**, 80–86 (2017).

11. Kalcheim, Y. *et al.* Robust Coupling between Structural and Electronic Transitions in a Mott Material. *Phys. Rev. Lett.* **122**, 57601 (2019).
12. Vardi, N. *et al.* Ramp-Reversal Memory and Phase-Boundary Scarring in Transition Metal Oxides. *Adv. Mater.* **29**, (2017).
13. Singer, A. *et al.* Nonequilibrium Phase Precursors during a Photoexcited Insulator-to-Metal Transition in V2 O3. *Phys. Rev. Lett.* **120**, 207601 (2018).
14. Als-Nielsen, J. & McMorrow, D. *Elements of X-Ray Physics, 2nd Edition*. (2011).
15. Moram, M. A. & Vickers, M. E. X-ray diffraction of III-nitrides. *Reports Prog. Phys.* **72**, (2009).
16. Warren, B. E. & Averbach, B. L. The effect of cold-work distortion on x-ray patterns. *J. Appl. Phys.* **21**, 595–599 (1950).
17. Williamson, G. K. & Hall, W. H. X-Ray broadening from filed aluminium and tungsten. *Acta Metall.* **1**, 22–31 (1953).
18. Chapman, H. N. *et al.* High-resolution ab initio three-dimensional x-ray diffraction microscopy. *J. Opt. Soc. Am. A* **23**, 1179 (2006).

# BIOGRAPHICAL SKETCH

Ziming Shao received a bachelor's degree (2017) in the field of Inorganic Nonmetallic Materials Engineering from the University of Science and Technology Beijing. After that, he went to United States and continued to pursue a master's degree in Materials Science and Technology at Cornell University.

# ACKNOWLEDGMENTS

I would like to present my greatest gratitude to my parents, Feng Shao and Fei Chen, who raised me with love and care. They always pay great attention to my education and work hard to provide me opportunities to make choices. It's them who bring me here today. Many thanks!

I'm grateful to my advisor, Professor Andrej Singer, who shared his extensive knowledge selflessly and guided me patiently and carefully. I'm also grateful to all the members of our group, Oleg, Daniel, Ryan, Ziyi, Vincent, and Yifei. They supported and helped me to overcome many obstacles in the two years of my master's study.

Last but not least, I want to acknowledge Yoav Kalchheim and Jacob Ruff, who have great contributions to the completion of this study. The $V_2O_3$ thin films are prepared by Yoav, and he always shared his research progress with us generously. And Jacob carefully assisted and supported to prepare and perform our X-ray diffraction experiment at CHESS.

Ziming Shao

July 2019